UC Berkeley
UC Berkeley Previously Published Works

Title
Failure processes of a gradient 2D-braided SiC-based nuclear-fuel cladding material at room temperature and 1200°C: an in situ X-ray tomography study

Permalink
https://escholarship.org/uc/item/7xg7m5z2

Journal
Composites Part B Engineering, 329

ISSN
1359-8368

Authors
Yuan, Guanjie
Zhang, Qiance
Lahoda, Edward
et al.

Publication Date
2027

DOI
10.1016/j.compositesb.2026.114300

Copyright Information
This work is made available under the terms of a Creative Commons Attribution License, available at https://creativecommons.org/licenses/by/4.0/

Peer reviewed

eScholarship.org Powered by the California Digital Library
University of California

Composites Part B 329 (2027) 114300

Contents lists available at ScienceDirect

Composites Part B

journal homepage: www.elsevier.com/locate/compositesb

Failure processes of a gradient 2D-braided SiC-based nuclear-fuel cladding material at room temperature and 1200°C: an *in situ* X-ray tomography study

Guanjie Yuan [a,b,*], Qiance Zhang [a,b], Edward Lahoda [c], Toshiki Nishimura [d], Masaru Ukai [d], Toshiaki Takada [d], Peng Xu [e], Robert O. Ritchie [f,g], Dong Liu [a,b,**]

[a] Department of Engineering Science, University of Oxford, Oxford, UK
[b] School of Physics, University of Bristol, Bristol, UK
[c] Westinghouse Electric Company LLC, Churchill, PA, USA
[d] Isogo Nuclear Engineering Centre, Toshiba Energy Systems & Solutions Corporation, Yokohama, Japan
[e] Post Irradiation Examination, Idaho National Laboratory, Idaho, USA
[f] Department of Materials Science & Engineering, University of California Berkeley, BA, USA
[g] Materials Sciences Division, Lawrence Berkeley National Laboratory, Berkeley, CA, USA

ARTICLE INFO

Keywords:
Ceramic-matrix composite
Accident tolerant fuel
X-ray computed micro-tomography
Deformation and fracture
SiC coating

ABSTRACT

Continuous SiC-fibre-reinforced SiC-matrix composites (SiC_f-SiC_m CMCs) with SiC coatings are widely considered as candidate accident-tolerant fuel cladding materials for advanced light-water reactors. In this work, a four-layer gradient braided SiC_f-SiC_m cladding material with a bilayer outer SiC coating was investigated under C-ring compression at room temperature (RT) and 1200°C in argon (Ar) using *in situ* X-ray micro-computed tomography (XCT). Two specimens were tested at each temperature. The mean maximum nominal hoop stresses were 77.3 ± 2.7 MPa at RT and 80.5 ± 7.3 MPa at 1200°C (mean ± standard deviation), indicating comparable peak nominal stress levels within the limited specimen set. The inner coating sub-layer exhibited a more pronounced columnar-grain morphology approximately normal to the coating surface, whereas the outer sub-layer showed less clearly aligned columnar features. Crack deflection was repeatedly observed near the interface between the two coating sub-layers under C-ring loading. Within the braided CMC layer, XCT-resolvable cracks underwent redirection and bifurcation and were arrested near fibre-bundle interfaces, and no XCT-resolvable through-thickness crack was observed within the investigated volume at either temperature. A four-stage failure-process model is proposed based on the *in situ* XCT observations. Hermeticity was not evaluated, and the observed crack morphology should not be interpreted as evidence of retained gas tightness or functional cladding integrity.

1. Introduction

Continuous nuclear-grade silicon carbide (SiC) fibre reinforced SiC matrix composites (SiC_f/SiC_m) possess many advantages, *e.g.*, low neutron absorption cross-section and high mechanical strength at elevated temperatures [1–5]. These attributes make SiC_f/SiC_m an attractive candidate accident-tolerant fuel (ATF) cladding material for advanced light-water reactors (LWRs), particularly for improving tolerance under beyond-design-basis accident scenarios such as loss-of-coolant accidents (LOCAs) and station blackouts [5–12].

The manufacturing process of such cladding material typically involves several sequential steps as follows (i) highly crystalline continuous SiC fibres (*e.g.*, HI-NICALON™-Type-S fibres [6,7], [13]): are bundled into a fibre tow, and then braided around a cylindrical mandrel [14]; (ii) a thin layer of pyrolytic carbon (PyC) coating is applied to the fibres via chemical vapor deposition (CVD) process, which facilitates fibre sliding and pull-out [15,16], and consequently enhances the (pseudo) ductility of the entire cladding; (iii) high-purity SiC matrix is deposited onto the structure (commonly via chemical vapor infiltration (CVI)) method to densify the cladding tube structure, enhancing its

* Corresponding author. Department of Engineering Science, University of Oxford, Oxford, UK.
** Corresponding author. Department of Engineering Science, University of Oxford, Oxford, UK.
E-mail addresses: pl19178@bristol.ac.uk (G. Yuan), dong.liu@eng.ox.ac.uk (D. Liu).

https://doi.org/10.1016/j.compositesb.2026.114300
Received 13 August 2026; Received in revised form 30 September 2026; Accepted 10 October 2026
Available online 12 October 2026
1359-8368/© 2026 The Authors. Published by Elsevier Ltd. This is an open access article under the CC BY license (http://creativecommons.org/licenses/by/4.0/).

mechanical properties and resistance to irradiation damage [6]; (iv) dense CVD monolithic SiC coatings are applied onto the outer surface of the cladding material (hereafter referred to as 'outer SiC coating' in the following text) to enhance the hermeticity of the material system [8].

For such a complex material system, the architecture of the SiC-fibre reinforcement, including the fibre-bundle orientation and braiding pattern, can strongly influence the mechanical response and damage evolution of SiC_f/SiC_m composites [17–19]. Several fibre architectures have been developed for tubular SiC_f/SiC_m cladding, including one-dimensional (1D) filament winding, conventional two-dimensional (2D) woven architectures [20]; modified 2D architectures containing additional fibre bundles oriented preferentially along the axial or hoop direction, and three-dimensional (3D) braided architectures with interlaced or orthogonally arranged fibre bundles [21]. Recent studies have referred to such through-thickness variation in layer-specific braid angles as gradient or asymmetric 2D braiding [20], [22]. However, the influence of fibre architecture cannot be represented by a universal strength ranking, because the mechanical response additionally depends on the loading direction, fibre-bundle orientation, fibre volume fraction, matrix porosity and fibre/matrix interfacial characteristics [23–25]. Importantly, the effects of fibre architecture should also be considered separately for different loading modes. Under tensile loading, progressive matrix cracking, interfacial debonding and sliding, load redistribution to the reinforcing fibres, and eventual fibre fracture are important components of the damage processes, with the response being strongly dependent on the orientation of the fibre bundles relative to the loading direction [22,23]. In contrast, flexural loading introduces a through-thickness stress gradient and may activate different damage processes on the tensile and compressive sides, including matrix cracking, fibre-bundle damage and local compressive cracking [26,27]. For instance, Zhao et al. [28] reported that, for their particular KD-I SiC-fibre-reinforced system under room temperature (RT) three-point bending, the 3D-braided composite exhibited a higher flexural strength (~323.1 MPa) and fracture toughness (~11.2 MPa $\sqrt{m}$) than the advanced 2D-braided composite (~188.3 MPa and ~5.7 MPa $\sqrt{m}$, respectively). This comparison demonstrates that fibre architecture can significantly affect the flexural response of a particular SiC_f/SiC_m system, but it should not be interpreted as establishing a universal ranking of flexural or tensile properties among different architectures. Accordingly, literature comparisons among conventional 2D, gradient 2D-braided and 3D architectures are used here only as contextual mechanistic comparisons rather than as evidence of a universal mechanical-property ranking.

In addition to the architecture of the CMC layer, the outer CVD SiC coating represents another structural level that can govern the initiation and subsequent evolution of damage in SiC_f/SiC_m cladding. Dense outer CVD SiC coating is applied on the SiC_f/SiC_m to improve its hermeticity [8], [29–32]. Because the maximum tensile stress under C-ring compression occurs at the outer surface, cracking can initiate within this relatively brittle monolithic coating before interacting with the underlying heterogeneous CMC layer [2,3]. The microstructure and interfaces within the coating can therefore influence not only the onset of cracking but also the subsequent crack path before the crack reaches the coating/CMC interface. The deposition conditions used for CVD SiC can substantially modify the coating microstructure and mechanical properties. For example, Drieux et al. [33] reported that the addition of propylene to the precursor gas promoted SiC crystallization and altered the mechanical response of monolithic CVD SiC tubes under C-ring compression. Their material produced with propylene addition exhibited a higher RT strength (~610 MPa) than the corresponding reference material (~364 MPa). These observations demonstrate that the microstructure of the outer coating can significantly influence coating fracture behaviour. More importantly, in a coated SiC_f/SiC_m cladding system, coating cracks may subsequently interact with internal coating interfaces, the coating/CMC interface and the heterogeneous fibre architecture beneath. Understanding this sequential crack transfer is therefore essential for interpreting the failure of the complete coated system. Therefore, the present work includes detailed characterization of the outer SiC coating (*e.g.*, microstructures and local properties) for the interpretation of the mechanical behaviour and failure process of coated SiC_f/SiC_m claddings.

Previous XCT-based investigations have enabled direct 3D characterization of internal pores, cracks and progressive damage evolution [18], [34]. In particular, recent *in situ* synchrotron XCT studies of SiC_f/SiC_m cladding under C-ring compression [2,3] have revealed the sequence of crack initiation and propagation within coated composite structures, including the interaction between cracks, coatings and heterogeneous fibre architectures. However, the transfer of damage from a bilayer coating, across the coating/CMC interface and into a gradient braided substrate has not been resolved.

The C-ring configuration is particularly useful for such *in situ* studies because circumferential loading is relevant to tubular fuel cladding, for which differential pressure across the cladding wall, including internal rod gas pressure, can generate tensile hoop stresses on the outermost surface of the cladding during service and transient conditions [35]. Under diametral compression, bending of the C-ring produces a maximum tensile circumferential stress near the outer surface, providing a simple and experimentally accessible configuration for examining hoop-oriented damage evolution by synchrotron XCT imaging [31], [36,37]. It should be noted that C-ring compression does not reproduce the membrane-type stress distribution generated by direct internal pressurisation of an intact tube; rather, it provides a practical surrogate loading configuration for investigating damage evolution under a controlled circumferential tensile stress field.

High-temperature characterization is particularly important because the deformation, interfacial response and fracture processes of SiC-based cladding may differ from those observed at RT. In the present work, 1200°C was selected as an accident-relevant high-temperature benchmark, close to the historically used 1204°C (2200 °F) peak-cladding-temperature criterion for LOCA assessment of conventional zirconium-alloy cladding [38,39]. This temperature also maintains consistency with our previous *in situ* XCT studies of 3D-braided SiC_f/SiC_m cladding with monolithic or multilayer outer SiC coatings tested under the same RT/1200°C C-ring framework [2], [3], thereby enabling contextual comparison under a consistent experimental temperature. The present material, however, combines an advanced bilayer CVD-SiC outer coating with an internal sub-layer interface and a four-layer gradient 2D-braided CMC substrate containing different fibre-bundle orientations through the wall-thickness. It therefore remains to be established how cracks initiate and evolve across the coating sub-layer interface and coating/CMC interface, and how their subsequent propagation, deflection and arrest within the CMC substrate are affected by temperature.

To address this gap, *in situ* synchrotron XCT was used to track progressive damage under C-ring compression at RT and 1200°C in Ar, supported by scanning electron microscopy (SEM), Raman spectroscopy and nanoindentation. Particular attention was given to the transfer of XCT-resolvable cracks from the bilayer coating, across coating interfaces and into the gradient 2D-braided CMC substrate. The fundamental contribution is therefore the spatially resolved hierarchical crack-transfer sequence across these structural levels and its variation with temperature. Comparison between RT and 1200°C further enables the role of temperature in modifying this hierarchical crack-evolution process to be assessed.

2. Materials and experimental procedures

2.1. Materials and sample preparation

In this study, the nuclear-grade SiC_f/SiC_m cladding materials were manufactured and provided by Toshiba Energy Systems & Solutions Corporation. Detailed manufacturing parameters beyond the material/

architecture information reported here are proprietary to the supplier and were not available to the authors. Bulk density and uniaxial tensile strength were not measured in the present study. The HI-NICALON™-Type-S fibres form a four-layer gradient 2D-braided CMC architecture. From the outer to inner CMC region, the fibre-bundle orientations are +60°, −60°, 90° and +60°, respectively, with respect to the hoop direction of the cladding (see Section 3.1). Here, the term "gradient" refers to the through-thickness variation in fibre-bundle orientation among the individual layers rather than a monotonic angular gradient [20], [22]. The inner radius (r_i), outer radius (r_o) and wall-thickness (t) of the cladding were determined through XCT imaging, yielding values of $r_i = 3.98 \pm 0.14$ mm, $r_o = 4.83 \pm 0.12$ mm and $t = 0.85 \pm 0.017$ mm (mean ± standard deviation (SD) of the geometric measurements), the average r_i/r_o ratio is ~0.82. C-ring specimens were prepared using a CUTLAM®1.1 manual cutting machine with a water-based coolant following the procedure described in Ref. [2]. For nanoindentation measurements, the as-received materials and post-tested materials at RT and 1200°C in Ar were mounted by a BUEHLER SimpliMet™ XPS1 hot compression mounting apparatus with 3 MPa pressure and a temperature of 220°C (heating and cooling time of 3 min). Detailed polishing and grinding procedures can be found in Ref. [2].

2.2. Scanning electron microscopy, Raman spectroscopy and nanoindentation

Scanning electron microscopy (SEM) characterization was performed using a Zeiss Evo MA10 LaB6 microscope operated in backscattered-electron (BSE) mode at 20 kV, 62 μA and a working distance of ~12.5 mm. Raman measurements were performed on polished cross-sections of the as-received material as a complementary microstructural characterization method to identify SiC- and carbon-related spectral features and to qualitatively compare the Raman response of the two outer-coating sub-layers. A Renishaw InVia micro-Raman system with a 488 nm laser operated in confocal mode was used. A long-working-distance 50× objective provided a laser spot of approximately 0.6–0.7 μm at an incident power of ~20 mW. Spectra were acquired over 200–1800 cm^{-1}, with an acquisition time of 20 s. The calibration and peak-analysis procedures followed our previously reported methodology [3], [40]. Raman data in the present work are used for qualitative phase and structural comparisons rather than for residual-stress determination or absolute crystallinity quantification.

Nanoindentation tests were performed on polished cross-sections of the as-received and post-tested materials (sample J1 at RT and J3 at 1200°C) using a Hysitron TI Premier nanoindenter equipped with a Berkovich diamond tip. The same indentation protocol as reported previously [2], [40] was used, with depth-controlled loading to 500 nm, loading/unloading rates of 100 nm/s, a 2 s hold at maximum depth, and a minimum spacing of 10 μm between neighbouring indents. The hardness (H) and elastic modulus (E) were subsequently obtained via the Oliver and Pharr method [41]. More than 50 local indentation measurements were obtained for each constituent and condition, with the detailed sampling numbers, statistical treatment and 95% confidence intervals provided in Table S2 in the Supplementary Materials.

2.3. High temperature C-ring compression tests with in situ X-ray tomography imaging

2.3.1. In situ C-ring compression tests

In situ high-temperature C-ring compression tests combined with synchrotron XCT imaging were performed at beamline 8.3.2 of the Advanced Light Source at the Lawrence Berkeley National Laboratory (USA). As shown in Fig. 1, a compressive load was applied to the C-ring specimen by alumina ceramic plates. Based on the ASTM Standard C1323-16 [42], nominal C-ring hoop stress at the outer tensile surface (σ_{ymax}) can be estimated via Eq. (1):

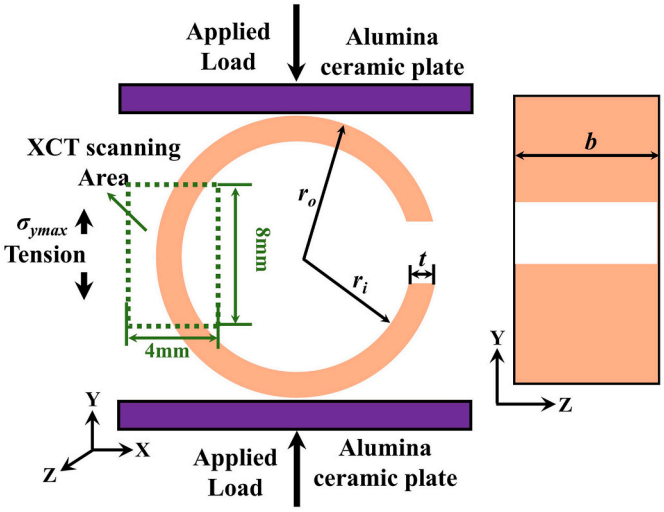


Fig. 1. Schematic representation of the C-ring compression loading configuration to illustrate the coordinate system along with a typical sample geometry (X is the radial direction; Y is the hoop direction, and Z is the axial direction of the cladding tube). XCT scans, illustrated by dashed rectangles (field of view: 8 × 4 mm), were acquired near the region of maximum nominal tensile hoop stress in the C-ring configuration.

$$\sigma_{ymax} = \frac{P_U R}{b t r_o}\left[\frac{r_o - r_a}{r_a - R}\right], \tag{1}$$

where P_U is the peak load, b is the effective C-ring width used for stress calculation, the terms R and the average radius r_a can be defined by Eqs. (2) and (3), respectively, according to the ASTM C1323-16 [42].

$$R = \frac{r_0 - r_i}{ln\frac{r_o}{r_i}}, \tag{2}$$

$$r_a = \left(\frac{r_o + r_i}{2}\right), \tag{3}$$

Specimen-specific dimensions are provided in Table S1 in the Supplementary Materials. The value calculated from Eq. (1) is treated as a nominal C-ring hoop stress. Because diametral compression produces a bending-dominated through-thickness stress gradient, it should not be interpreted as the uniform membrane hoop stress of an internally pressurised tube or as the exact local stress in an individual coating layer.

C-ring loading was performed using the previously described high-temperature *in situ* XCT rig [43], [44] in displacement-control mode. A preload of ~5 N was applied, followed by quasi-static loading at ~0.5 μm/s with a minimum displacement increment of 0.1 μm. Heating was provided by six infrared halogen lamps, and specimen temperature was monitored using a thermocouple attached to the outer C-ring surface. High-temperature tests were conducted once the temperature stabilized at 1200 ± 5°C. The principal RT and 1200°C tests were conducted in high-purity Ar to provide a non-oxidizing baseline. In addition, two specimens were tested at 1200°C in air using the same C-ring loading and interrupted *in situ* XCT procedure as an environmental-sensitivity comparison; because the principal scope of the present study is the RT/1200°C comparison under non-oxidizing Ar, the detailed air-test results are provided in the Supplementary Materials.

A white light X-ray beam (6 to 43 keV) was used to capture 3D tomography images. These images, obtained as the instrument rotates through 180°, were converted to visible light by a scintillator and recorded using a high-resolution CCD camera. This setup produced a pixel size of 3.25 μm × 3.25 μm and an 8 mm × 4 mm field of view (FOV), centred on the area of maximum hoop stress in the C-ring samples (Fig. 1). Considering the imaging conditions and material contrast,

the XCT measurements enabled identification of major crack features with dimensions above the effective spatial resolution limit of the system. The selected pixel size represents a compromise between spatial resolution and FOV. A higher spatial resolution would improve the detection capability for smaller features but reduce the observable volume, whereas a lower spatial resolution would limit the ability to resolve coating cracks. Therefore, the selected XCT configuration enabled characterization of coating crack evolution while maintaining a sufficiently large observation volume for tracking deformation and damage development.

Each scan consists of 1969 projections, with a total acquisition time of ~10 min. Approximately seven XCT scans were collected for each sample at increasing loading steps, including one pre-load scan for microstructural analysis of as-received materials.

2.3.2. Processing for 3D visualization of XCT scans

The reconstruction of XCT images were conducted by using the Gridrec algorithm [45] in the TomoPy package [46]. For each scan, the rotation centre was manually identified, and flat field correction was applied to enhance spatial resolution and minimize detector noise. The reconstructed scans were converted to stacks of 32-bit TIFF images, processed in ImageJ software for contrast adjustment to a fixed dynamic range (−5.6 to 2.8), and saved as 8-bit '.raw' data files to reduce computational and storage requirements while maintaining sufficient grey-scale contrast for the subsequent segmentation and crack-analysis procedures. This procedure has been widely adopted in XCT-based investigations of heterogeneous materials, *e.g.*, SiC-based CMCs [47], oxide-oxide aerospace CMCs [48] and nuclear-graphite [49]. To ensure spatial consistency between different interrupted loading stages, all reconstructed XCT scans acquired from the same specimen were registered to the pre-loading XCT scans using the Image Registration Module in Avizo Lite software (version 2019.4). The registration procedure was performed to compensate for rigid body displacement during interrupted C-ring compression and to establish spatial correspondence among the XCT datasets. This registration-based approach has been widely adopted for analysing *in situ* high-temperature XCT datasets and has been successfully applied to various material systems, *e.g.*, SiC-based CMCs [47], oxide-oxide aerospace CMCs [48] and nuclear-graphite [49].

For pore segmentation and 3D connectivity analysis, the registered pre-load XCT volume of each specimen was imported into Avizo Lite (version 2019.4). Pore voxels were identified using the Image Segmentation Module based on the grey-level contrast between pore and solid regions. Because the reconstructed grey-level distributions varied slightly among individual SiC-based CMC datasets, the segmentation threshold was selected according to the pore/solid contrast of each dataset rather than by applying a single universal threshold [2], [3]; the settings used in the present analyses typically fell within an approximate 8-bit grey-level range of 16–171. A three-iteration median filter was subsequently applied as part of the pore-segmentation procedure. The detailed segmentation procedure can be found in Ref. [2] with one example presented in Fig. S1 in the Supplementary materials. To examine the 3D connectivity of the inter-bundle macropores, the segmented macropore mask generated in Avizo was subsequently imported into Dragonfly 2021.1 (Build 977). Dragonfly was not used to re-segment the original grey-scale XCT data; instead, the Analysing Connected Components module was used to separate the existing macropore mask into individual three-dimensional connected clusters using a 26-connected voxel-neighbourhood criterion. Under this criterion, segmented pore voxels sharing a face, edge or corner were considered connected. The resulting component labels were used to visualize the 3D connectivity of the inter-bundle macropore network. The detailed segmentation workflow and threshold-sensitivity analysis are provided in the Supplementary Materials, including Fig. S2.

Crack identification was performed by correlating XCT observations with the mechanical response and damage evolution during interrupted C-ring compression. The initial XCT volume (pre-load scan) was first analysed to identify and reconstruct pre-existing pore structures, which were used as a reference for subsequent crack evolution analysis. During the early loading stages near crack initiation, the specimen deformation was limited, allowing spatial correlation between the pore map and corresponding XCT volumes through image overlap. Newly generated XCT-resolvable cracks were identified based on their absence in the initial state, appearance after loading and connection with newly developed crack regions. Under the present C-ring compression configuration, the first XCT-resolvable cracks were observed within the outer CVD-SiC coating. Therefore, early-stage crack evolution was tracked from these initial coating cracks and their interaction with surrounding structural features. At higher loading stages, significant specimen deformation reduced the reliability of direct image overlap; therefore, crack identification was based on 3D continuity and progressive propagation behaviour. The detailed workflow (Fig. S3 and S4) are provided in the Supplementary Materials.

3. Results

This section presents the results for (i) microstructures of both as-received materials and post-tested materials, (ii) characterization of local properties of individual components in both as-received materials and post-tested materials, (iii) mechanical behaviour at RT and 1200°C, and (iv) failure processes at RT and 1200°C.

3.1. Microstructure of as-received materials

Typical microstructure of the as-received material is presented in Fig. 2a. The average thicknesses of outer SiC coating and CMC layer were measured to be 123.80 ± 5.62 μm and 725.84 ± 10.19 μm, respectively. In the outer SiC coating, the interface between the two sub-layers (named as 'layer one' and 'layer two') was marked by a dashed straight line for visual guidance, but note that the interface is not necessarily along a straight line as evidenced by interfacial closed pores at varied distances away from straight line (marked by green arrows, Fig. 2b). Both sub-layers have a thickness of ~60 μm, Fig. 2b. Specifically, larger columnar grains were found in layer one oriented between 0° and 20° relative to the radial direction of the cladding. However, SiC grains in layer two exhibited less well-aligned orientations (in the range of 0° to 85° relative to the radial direction), Fig. 2b. The description of grain alignment is based on morphological observations from polished cross-sectional SEM images and does not represent a crystallographic-orientation measurement. No diffraction-based texture analysis was performed in the present study. Furthermore, Raman spectra for layer one showed three sharp TO peaks (at ~ 765 cm^{-1}, ~785 cm^{-1} and ~ 798 cm^{-1}) and one LO peak (at ~ 973 cm^{-1}), Fig. 2c. However, in layer two, significant broadening of TO and LO peaks were observed, indicating a qualitative difference in the local SiC spectral response, Fig. 2d.

In the underlying CMC substrate, the fibre bundles form a four-layer (I to IV) gradient 2D-braided architecture: layer I at +60°, layer II at −60°, layer III at 90°, and layer IV at +60° with respect to hoop direction (Y direction), Fig. 3a.

Two types of pores were distinguished according to their microstructural locations rather than by applying a pore-size cutoff: macropores were located between neighbouring fibre bundles, whereas micropores were located within fibre bundles, primarily in the matrix between individual fibres. The 26-connected-component analysis revealed substantial 3D connectivity among the inter-bundle macropores (Fig. 3b), including connections across the layer-II/layer-III and layer-III/layer-IV regions. The macropore volume fraction was measured to be 3.27 ± 0.17 vol%, compared with 6.32 ± 0.46 vol% for micropores, giving a total porosity of 9.64 ± 0.29 vol%, where the uncertainties represent the SD across the analysed pre-load XCT volumes. As demonstrated by the threshold-sensitivity analysis in the Supplementary Materials, the absolute segmented macropore fraction is

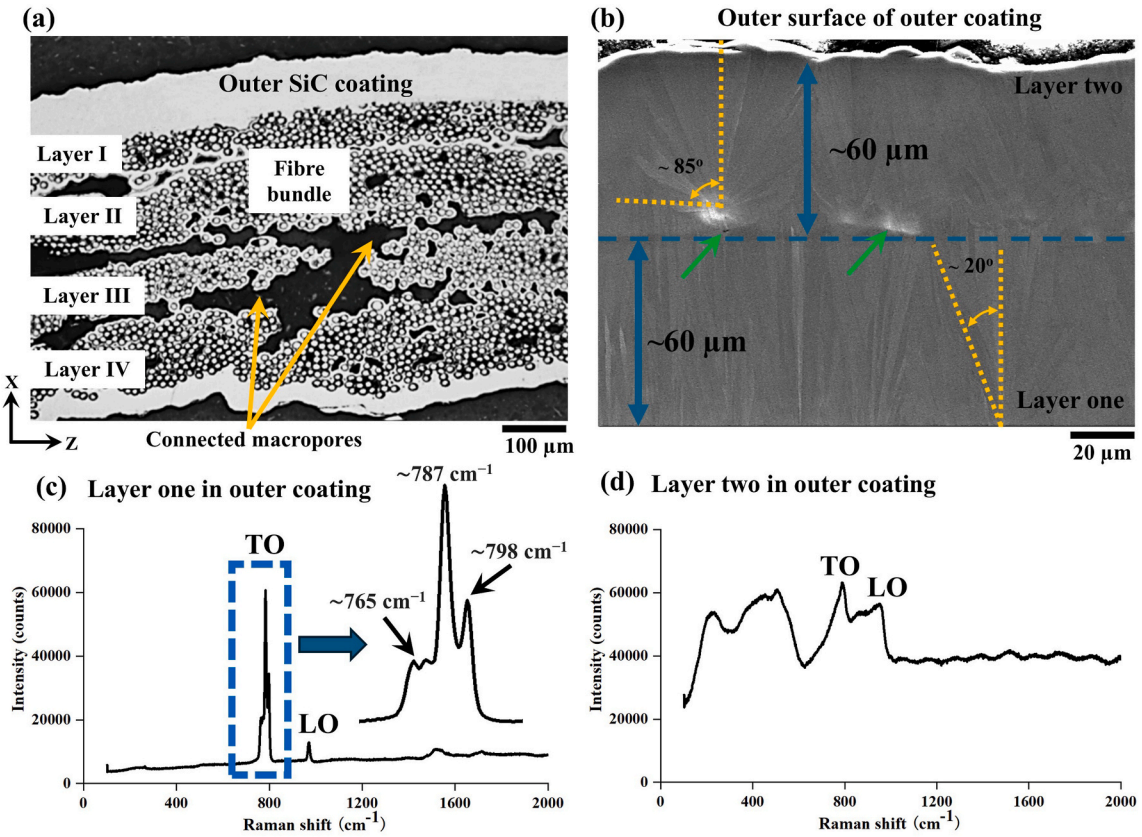


Fig. 2. (a) SEM image from the polished cross-sections (of X-Z plane) of the as-received material, showing the typical microstructures. (b) SEM image of outer SiC coating with two sub-layers, with closed interfacial pores marked by green arrows and the orientation of SiC grains marked by dashed lines. (c) and (d) are typical Raman spectra collected in layer one and layer two of the outer SiC coating, respectively. (For interpretation of the references to colour in this figure legend, the reader is referred to the Web version of this article.)

dependent on threshold selection; these values are therefore used as descriptive quantitative measures, whereas the principal feature considered here is the 3D connectivity of the inter-bundle macropore network. The PyC coatings were observed at the fibre/matrix interface area, as well as surrounding fibre bundles, Fig. 3c. For the post-tested materials at both RT and 1200°C, no obvious microstructural differences were observed, with results presented in Fig. S5 in the Supplementary Materials.

3.2. Local properties of individual components

Nanoindentation results for the as-received and post-tested materials are summarized in Table 1. The local properties measured in specimen J1 after RT testing were generally similar to those of the as-received material.

For the outer SiC coating, the average hardness (H) of as-received materials is ~29.90 GPa and it is uniform across the thickness for both sub-layers, Fig. 4a. There is ~7.7% increasing in the hardness (~32.2 GPa) for post-tested materials at 1200°C. As for the elastic modulus (E) of as-received material, it remains constant (~400 GPa) in layer one, *i.e.*, from the outer SiC coating/CMC substrate interface to ~60 μm distance away, and then steadily decreased to ~360 GPa (60-120 μm), Fig. 4b. For the post-tested materials at 1200°C, a similar trend was found: E is constant (~425 GPa) from CMC/coating interface to 60 μm distance away, and then steadily decreased to ~383 GPa at the surface of outer coating. The average E of outer coating for post-tested materials is ~418.9 GPa, which is ~6.1% higher than as-received materials (~394.9 GPa).

For the matrix between fibre bundles and matrix within a fibre bundle, they had similar local properties: ~30 GPa (H) and ~340 GPa (E) for as-received materials and there is about ~7% and ~9% increasing in H (~33 GPa) and E (~370 GPa) in post-tested material. For the SiC fibre, H and E values of as-received materials were measured to be ~16.8 GPa and ~187.7 GPa, and increased to ~17.8 GPa and ~196.2 GPa in post-tested materials. Note that the SiC fibre had a much lower (~55%) overall hardness and modulus values compared with other components. Overall, modestly higher local values were measured in J3 after the 1200°C test. Because these measurements represent local sampling of heterogeneous constituent regions and no thermally exposed but mechanically unloaded control was available, the differences are treated as descriptive post-test observations rather than statistically validated temperature-induced changes. Possible contributions from thermal exposure, damage and microstructural/residual-stress changes are considered in Section 4.2.

3.3. Nominal C-ring hoop stresses at coating-crack initiation and peak load

The load-time curves for C-ring compression tests were plotted in Fig. 5. Samples J1 and J2 were tested at RT; samples J3 and J4 were tested at 1200°C. For specimens tested under the same condition, the mechanical behaviour was found to be consistent. The detailed loading steps for these samples are tabulated in Table S1 in the Supplementary materials. Load drops were observed in all the tested samples (abrupt load-drop events, distinct from gradual load relaxation, were observed in all specimens and were associated with crack formation/propagation identified by XCT images in Section 3.4). Detailed load drops in all tested materials are listed in Table 2.

Samples J1 and J3 were selected as representative examples and load drops in their curves were marked by black arrows in Fig. 5. For all

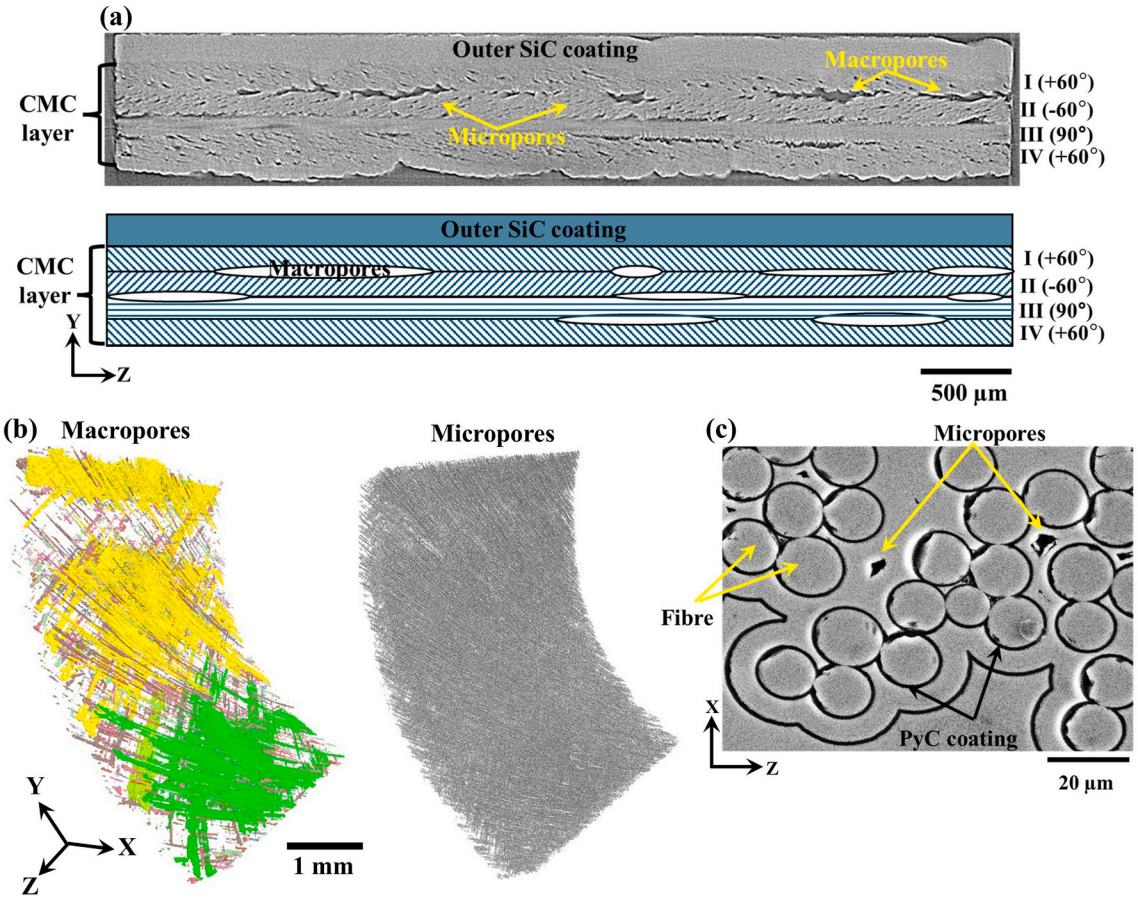


Fig. 3. (a) A representative XCT slice and corresponding schematic of Y-Z plane show four layers of fibre bundles in the CMC layer; (b) 3D visualization of macropores after 26-connected-component analysis, where each colour identifies an individual three-dimensionally connected macropore cluster; macropore voxels shown in the same colour belong to the same connected cluster, whereas different colours identify disconnected clusters. The colours are connectivity labels only and do not represent pore-size or pore-volume categories and 3D visualization of micro-size pores; (c) SEM image showing micropores and PyC interphase. (For interpretation of the references to colour in this figure legend, the reader is referred to the Web version of this article.)

Table 1
Measured hardness and elastic modulus values in different locations of the polished cross-section of SiC_f/SiC_m cladding materials in both as-received and post-tested (samples J1 and J3) conditions. Values are reported as mean ± standard deviation (SD) of the valid indentation measurements. The number of specimens, sampled regions and valid indents for each constituent/condition is provided in Table S2.

Locations	***H*** (GPa)			***E*** (GPa)		
	As-received	Post-tested at RT (J1)	Post-tested at 1200°C (J3)	As-received	Post-tested at RT (J1)	Post-tested at 1200°C (J3)
Outer SiC coating	29.90 ± 0.70	29.81 ± 0.63	32.20 ± 1.35	394.92 ± 15.29	390.13 ± 11.93	418.91 ± 17.00
Matrix within a fibre bundle	29.62 ± 2.73	29.97 ± 3.11	34.15 ± 1.89	339.45 ± 9.29	341.55 ± 8.07	369.55 ± 9.37
Matrix between fibre bundles	30.36 ± 0.93	30.76 ± 1.37	32.90 ± 1.97	340.51 ± 7.80	341.04 ± 7.17	373.17 ± 9.64
Fibre	16.78 ± 1.33	17.00 ± 2.01	17.80 ± 1.32	187.74 ± 9.92	186.07 ± 8.28	196.21 ± 9.10

tested materials, small load drops (0.7 N to 1.8 N) occurred before and at peak load (P_U), with the final large load drops (more than 5 N) occurred after peak load, Fig. 5. The first load drop was associated with the first XCT-resolvable outer-coating crack (Section 3.4). The nominal hoop stresses associated with outer-coating crack initiation were 52.78 and 56.97 MPa for J1 and J2 at RT and 42.30 and 39.56 MPa for J3 and J4 at 1200°C, corresponding to descriptive means of 54.9 ± 3.0 and 40.9 ± 1.9 MPa, respectively (mean ± sample SD, n = 2). Thus, the descriptive mean at 1200°C was approximately 25.5% lower than at RT. The corresponding maximum nominal hoop stresses were 79.20 and 75.32 MPa at RT and 85.66 and 75.31 MPa at 1200°C, giving means of 77.3 ± 2.7 and 80.5 ± 7.3 MPa, respectively. The peak nominal stress levels were therefore comparable within this limited specimen set. Because only two specimens were tested per condition, these comparisons are descriptive only; moreover, the peak-load-derived nominal stress may be influenced by stress redistribution following prior crack formation.

For each XCT acquisition, the specimen was held at a constant displacement for approximately 10 min. During these holding periods, progressive load relaxation was observed, particularly for specimens tested at 1200°C, and was clearly distinguishable from the abrupt load-drop events described above (Fig. 5). The specimen-specific testing sequence, including the load-drop events and the corresponding XCT acquisition time windows, is provided in Table S3, while the load relaxation during individual holding periods is quantified separately in Table S4. Because the load could evolve during the approximately 10-min acquisition, particularly at 1200°C, each XCT scan was labelled using the load recorded at the temporal midpoint of the corresponding acquisition window. This convention avoids assigning the scan either to the instantaneous load immediately following a load-drop event or to

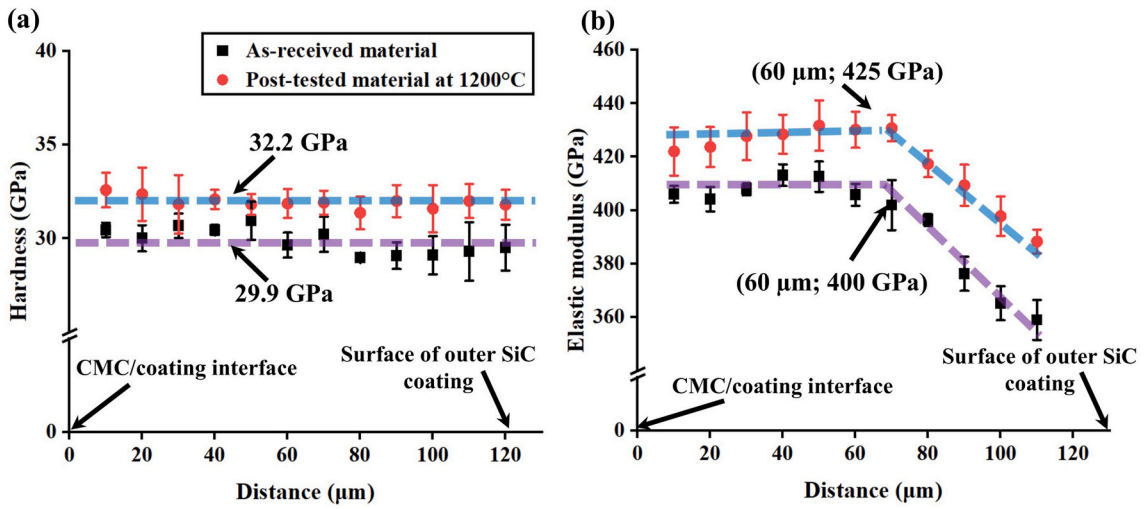


Fig. 4. Hardness and elastic modulus values across the thickness of outer SiC coating of polished cross-section of as-received materials and materials after testing at 1200°C. Dashed lines are for eye guidance only.

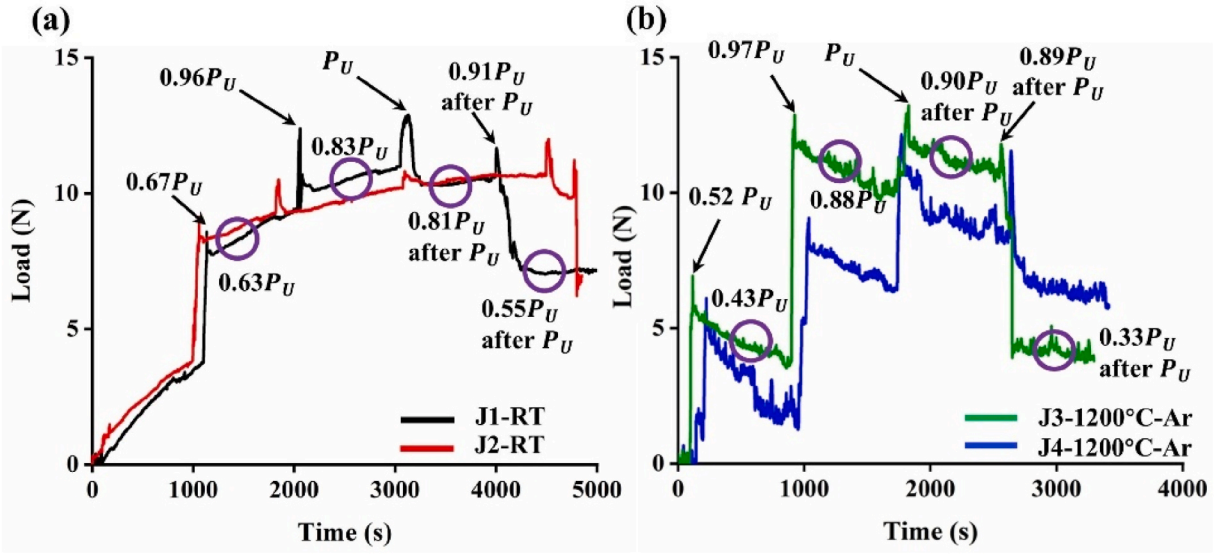


Fig. 5. Load-time curves for C-ring compression tests: (a) samples J1 and J2 tested at RT in Ar; (b) samples J3 and J4 tested at 1200°C in Ar. The open circles indicate locations of XCT scans on samples J1 and J3; load drops and peak load are marked by arrows in J1 and J3 curves.

Table 2
First load-drop events, peak loads, and corresponding nominal C-ring hoop stresses for specimens tested at RT and 1200°C in Ar.

Specimen	Load drop	First load drop/Nominal hoop stress corresponding to crack initiation in the outer SiC coating	Peak load/ Maximum nominal hoop stress
J1-RT-Ar	0.67 P_U; 0.96 P_U; P_U; 0.91 P_U after P_U	8.59 N/52.78 MPa	12.89 N/ 79.20 MPa
J2-RT-Ar	0.70 P_U; 0.87 P_U; 0.90 P_U; P_U; 0.92 P_U after P_U	9.13 N/56.97 MPa	12.07 N/ 75.32 MPa
J3-1200°C-Ar	0.52 P_U; 0.97 P_U; P_U; 0.89 P_U after P_U	6.92 N/42.30 MPa	13.23 N/ 85.66 MPa
J4-1200°C-Ar	0.46 P_U; 0.69 P_U; P_U; 0.98 P_U after P_U	6.11 N/39.56 MPa	12.32 N/ 75.31 MPa

the relaxed load at the end of the acquisition period.

3.4. Failure processes under C-ring compression loading

Samples J1 and J3 were chosen as illustrative examples at RT and 1200°C, respectively. The corresponding XCT observations for replicate specimens J2 and J4 are provided in Figs. S6 and S7, respectively, and show the same principal damage-evolution sequence at each corresponding temperature. Here, "crack initiation" denotes the first XCT-resolvable outer-coating crack; "coating cracking" denotes growth within the bilayer coating; "interfacial delamination" denotes crack extension along coating sub-layer, coating/CMC or fibre-bundle interfaces; "matrix cracking" denotes cracking through SiC matrix regions; and "fibre-bundle cracking" denotes crack penetration into a fibre-bundle region. The final stage refers to the final investigated post-peak damage state rather than complete wall failure. Specifically, crack penetration depth was evaluated from the XY plane of the specimen, which was selected because it exhibited relatively limited geometric distortion during C-ring compression compared with the other viewing

orientations. XCT datasets acquired at different loading stages were registered to the pre-loading XCT volume before crack-evolution analysis to compensate for rigid-body displacement and maintain spatial correspondence. All crack dimensions, penetration distances and crack–microstructure interactions reported in this section were evaluated within the registered XCT observation volume and within the spatial-resolution capability of the present imaging configuration. Therefore, the reported values refer specifically to XCT-resolvable crack features and do not exclude the possible presence of cracks below the XCT detection capability.

3.4.1. *Failure process for the materials tested at RT in Ar*

For RT sample J1, the XCT scan collected at 0.63 P_U after the first load drop revealed the formation of one primary coating crack, Fig. 6a. This crack extended across ~71% (~2.8 mm) of the sample width within the XCT field of view (~3.9 mm), with deflection visible on the coating surface (marked by open circles in Fig. 6a) as well as within the outer coating (Fig. 6b).

Note that, this deflection was located ~60 μm from the coating/CMC interface, coincident with the sub-layer interface shown in Fig. 2b. 3D visualization shows approximately 60% of the crack length remained within the outer coating, see example shown in XCT Slice 1, Fig. 6b. About 40% of crack length (~1.1 mm) simultaneously deflected along the coating/composite interface or travelled into the first layer of the fibre bundles, Slices 2 and 3 in Fig. 6b. With further loading to 0.83 P_U before P_U, the coating crack extended across the full observable width, with more crack deflection observed on the coating surface (marked by open circles), Fig. 7a. The width of crack on the coating surface increased with displacement as the load decreased (0.81 P_U after P_U in Figs. 7b and 0.55 P_U after P_U, Fig. 7c).

After peak load (scan collected at 0.81 P_U after P_U), instead of travelling across the thickness of the material, the XCT-resolvable crack either deflected or bifurcated in the CMC layer, Fig. 7d and e. The maximum observed crack depth occurred near the interface between fibre-bundle layers II and III of fibre bundles (Fig. 7d), which is ~60% of the total thickness of the material (~510 μm). Post peak load, the coating crack fronts also tended to deflect along the coating/CMC interface, leading to the delamination of outer SiC coating and the CMC layer, Fig. 7d and e. The propagating XCT-resolvable cracks were observed to intersect with interconnected macropore regions near the fibre-bundle interfaces. This spatial association is consistent with local redistribution of the crack path and crack-driving force, although the present observations do not isolate macropore connectivity as the sole cause of crack arrest, Fig. 7d and e. The replicate RT specimen J2 exhibited the same principal sequence, including outer-coating crack initiation and deflection, subsequent crack widening/penetration, and a final XCT-resolvable crack front remaining near the interface between fibre-bundle layers II and III (Fig. S6).

3.4.2. *Failure process for the materials tested at 1200°C in Ar*

At 1200°C, the first coating crack formed at a lower load (0.43 P_U) than at RT (0.63 P_U). Once formed, it travelled across the total width of the C-ring sample within the XCT field of view (~3.9 mm), which is different from the coating crack behaviour at RT, Fig. 8a. For this first coating crack, ~30% of crack length (~1.2 mm) either propagated into the CMC layer (marked by open rectangle in Fig. 8b) or deflected at the coating/CMC interface (Slice 1 and Slice 2 in Fig. 8b).

Similar to RT, crack deflection on the surface and within the outer

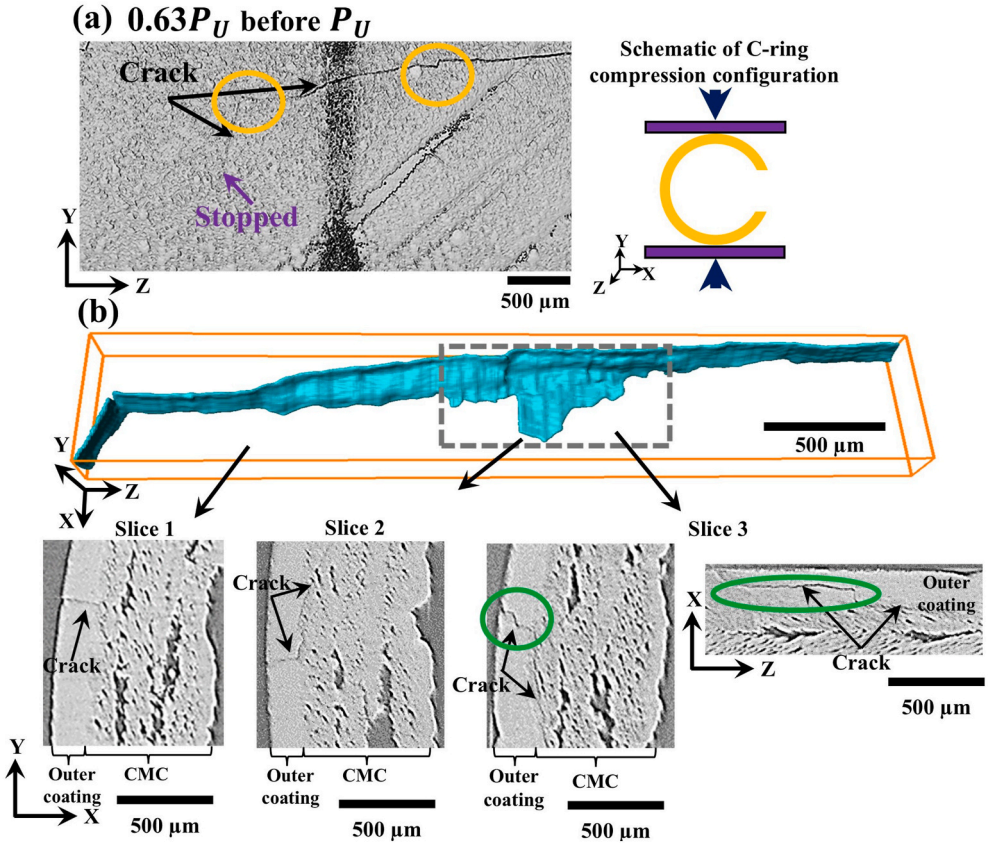


Fig. 6. 3D visualization of crack tested at RT at 0.63 P_U before P_U: (a) the YZ view shows crack deflection on the surface of outer coating (marked by orange open circle); (b) 3D visualization of coating crack from different views. Representative Slices 1 to 3 present different features of this coating crack: Slice 1 (XY view) for crack arrested at the coating/CMC interface; Slice 2 (XY view) for crack interacted with CMC layer; and Slice 3 (XY view and XZ view) for crack deflected in the coating (marked by green open circle). The viewing plane is indicated on the first panel of each image group; subsequent panels within the same group share the same orientation unless otherwise stated. (For interpretation of the references to colour in this figure legend, the reader is referred to the Web version of this article.)

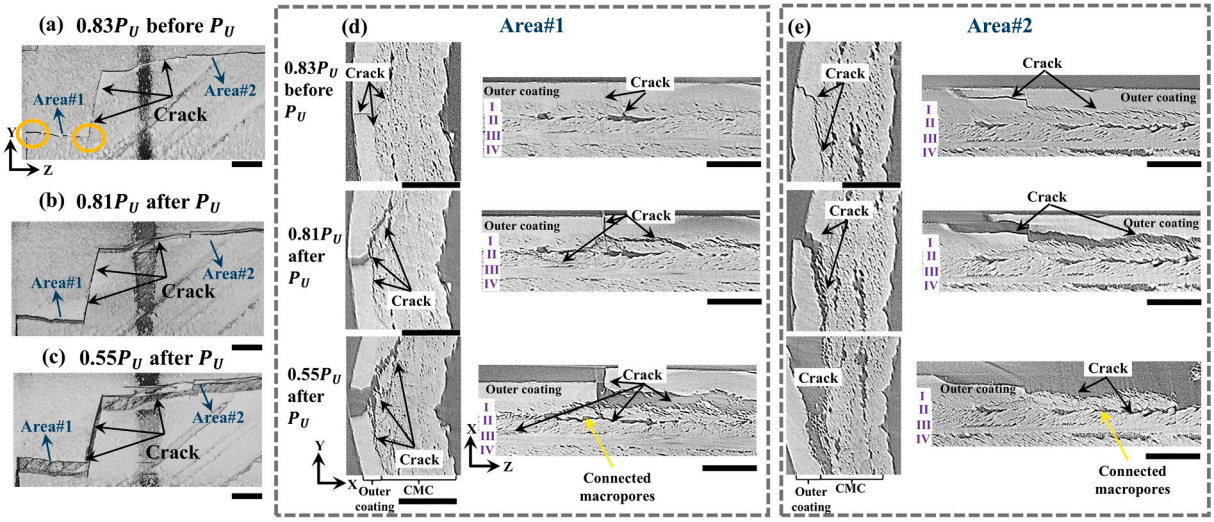


Fig. 7. Failure process at RT. (a) to (c) are XCT scans collected at 0.83 P_U before P_U, 0.81 P_U after P_U and 0.55 P_U after P_U of Y-Z plane; (d) and (e) are slices of X-Y plane and X-Z plane, respectively collected at two representative areas: Area#1 and Area#2, to illustrate the propagation depth of crack; Area#2 is the same area of Slice 3 in Fig. 6b. All scalebars are 500 μm. The viewing plane is indicated on either the first or last panel of each image group; subsequent panels within the same group share the same orientation unless otherwise stated.

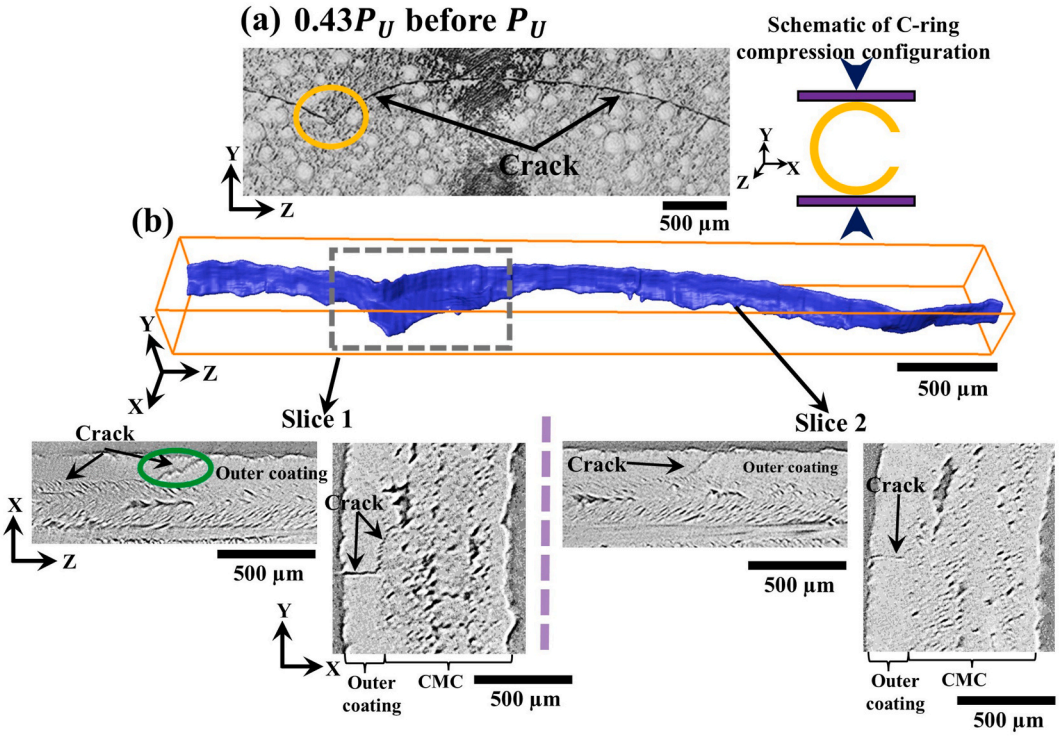


Fig. 8. Surface crack in the outer SiC coating at 1200°C at 0.43 P_U before P_U: (a) the YZ view shows crack deflection on the coating surface (marked by orange open circle). (b) 3D visualization of coating crack. Representative Slice 1: crack deflected in the outer coating (XZ view, marked by green open circle) and interacted with underlying composite (XY view); Slice 2: crack arrested at the coating/CMC interface. The viewing plane is indicated on either the first panel of each image group; subsequent panels within the same group share the same orientation unless otherwise stated. (For interpretation of the references to colour in this figure legend, the reader is referred to the Web version of this article.)

SiC coating were observed; the deflected location within the outer SiC coating was also ~60 μm away from the coating/CMC interface, Slice 1 (XZ view) in Fig. 9b.

As the load continued to increase, no obvious newly formed coating crack was observed under current XCT resolution, Fig. 9. Instead, the coating crack propagated deeper into the CMC layer, Fig. 9d and e. Similar to the observations at RT, no XCT-resolvable through-thickness crack was observed within the investigated volume even after reaching P_U (Fig. 9d and e). Crack deflection and local delamination were observed at the coating/CMC interface and within the fibre-bundle architecture. The maximum depth of crack at 1200°C is at the interface layer II and layer III of fibre bundles (~510 μm), Fig. 9d and e. The replicate 1200°C specimen J4 showed a closely consistent damage sequence, including outer-coating crack initiation and deflection,

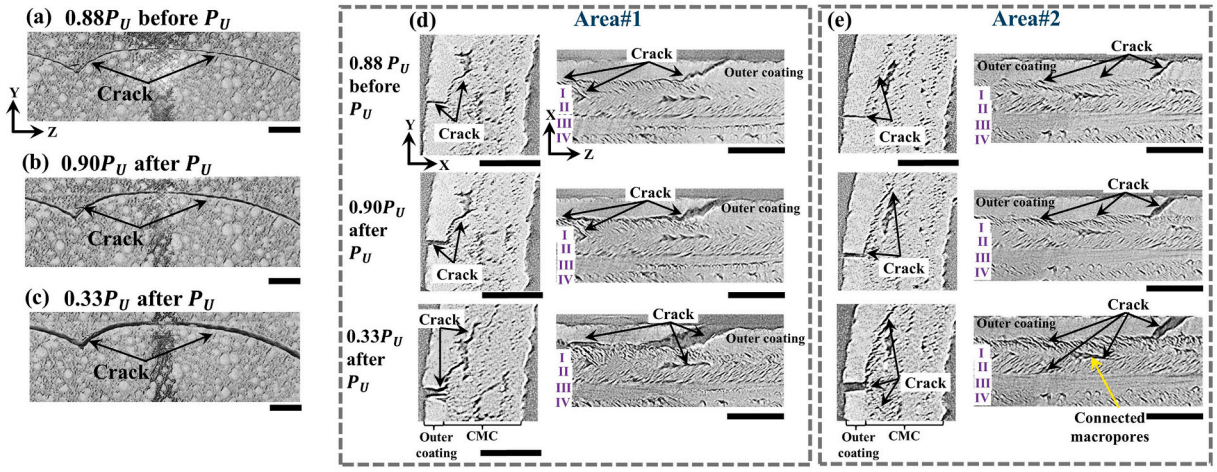


Fig. 9. Failure process at 1200°C: (a) to (c) are XCT scans collected at 0.83 P_U before P_U, 0.90 P_U before P_U and 0.33 P_U after P_U of Y-Z plane showing width of crack on the coating surface; (d) and (e) are slices of X-Y plane and X-Z plane, respectively collected at two representative areas: Area#1 and Area#2, to illustrate the propagation depth of crack. Area#1 is the same area of Slice 1 in Fig. 8b, and Area#2 is the same area of Slice 2 in Fig. 8b. All scalebars are 500 μm. The viewing plane is indicated on either the first panel of each image group; subsequent panels within the same group share the same orientation unless otherwise stated.

subsequent crack widening/penetration into the CMC, and a final XCT-resolvable crack front remaining near the interface between fibre-bundle layers II and III (Fig. S7). These quantitative observations provide direct evidence for the hierarchical crack-transfer behaviour from the bilayer CVD-SiC coating into the braided CMC substrate. Moreover, across all four specimens, the first XCT-resolvable damage in the outer coating was dominated by a single principal coating crack within the observed XCT window, and no spatially independent secondary coating cracks were subsequently identified away from this crack (Fig. S8 in the Supplementary Materials). Once the principal crack propagated into the CMC substrate, however, multiple secondary XCT-resolvable cracks and branches developed within the composite at subsequent loading stages. These secondary cracks remained spatially connected to the original coating-initiated crack, forming a branched damage network rather than multiple independently nucleated coating cracks (see Figs. 6–9 and Figs. S6 and S7).

At both temperatures, delamination of outer coating (Figs. 7 and 9), as well as fibre pull-out (Fig. 10) were observed. Notably, less extensive fibre pull-out was observed at 1200°C. Corresponding observations from replicate specimens J2 and J4 are provided in Fig. S9.

In the outer coating, the main toughening mechanism is crack deflection (Fig. 11a), with deflection on the outer coating surface and deflection inside outer coating.

In the underlying CMC layer, the crack toughening mechanisms could be classified into five types and were observed under all testing conditions, Fig. 11b. Crack deflection and bifurcation (Type I) were commonly observed, they happened simultaneously once crack reached the CMC layer, either along the CMC layer/outer coating interface or inside fibre bundles, Fig. 11b. Un-cracked ligament bridging (Type II, Fig. 11b) commonly occurred at crack tips when cracks reached the CMC layer, at both CMC layer/outer coating interface and inside fibre bundles. Tortuous crack pathways (Type III, Fig. 11b) occurred when cracks reached fibre bundles, with crack deflection and bifurcation along fibre/bundle interface and inside fibre bundles, as well as crack connections with macropores. Parallel cracks (Type IV, Fig. 11b) were commonly observed inside fibre bundles to diffuse the main crack and inhibit its further propagation. Fibre pull-out (Type V, Fig. 11b) commonly be observed after peak load, provide (pseudo) ductility of the cladding material. In summary, once crack reached the underlying CMC layer, Types I–IV mechanisms occurred simultaneously, with further loading to peak load, mechanisms of Type V happened.

4. Discussion

4.1. Microstructural features associated with crack evolution

The present outer SiC coating exhibits two microstructurally distinct sub-layers rather than a homogeneous through-thickness morphology. Layer one shows a more pronounced columnar-grain morphology, whereas layer two exhibits less clearly aligned grains and broader SiC Raman bands (Fig. 2). The Raman spectra showed differences in the shape/broadening of the SiC TO band between the two coating sub-

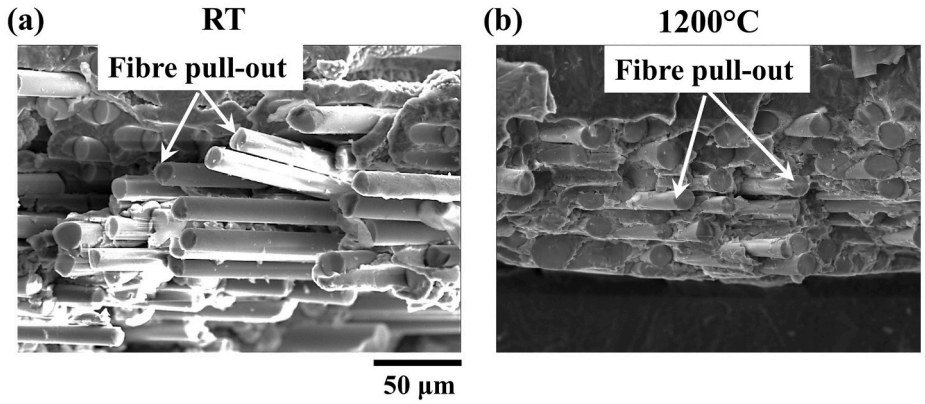


Fig. 10. SEM images showing fibre pull-out of the post-tested materials: (a) at RT, (b) at 1200°C.

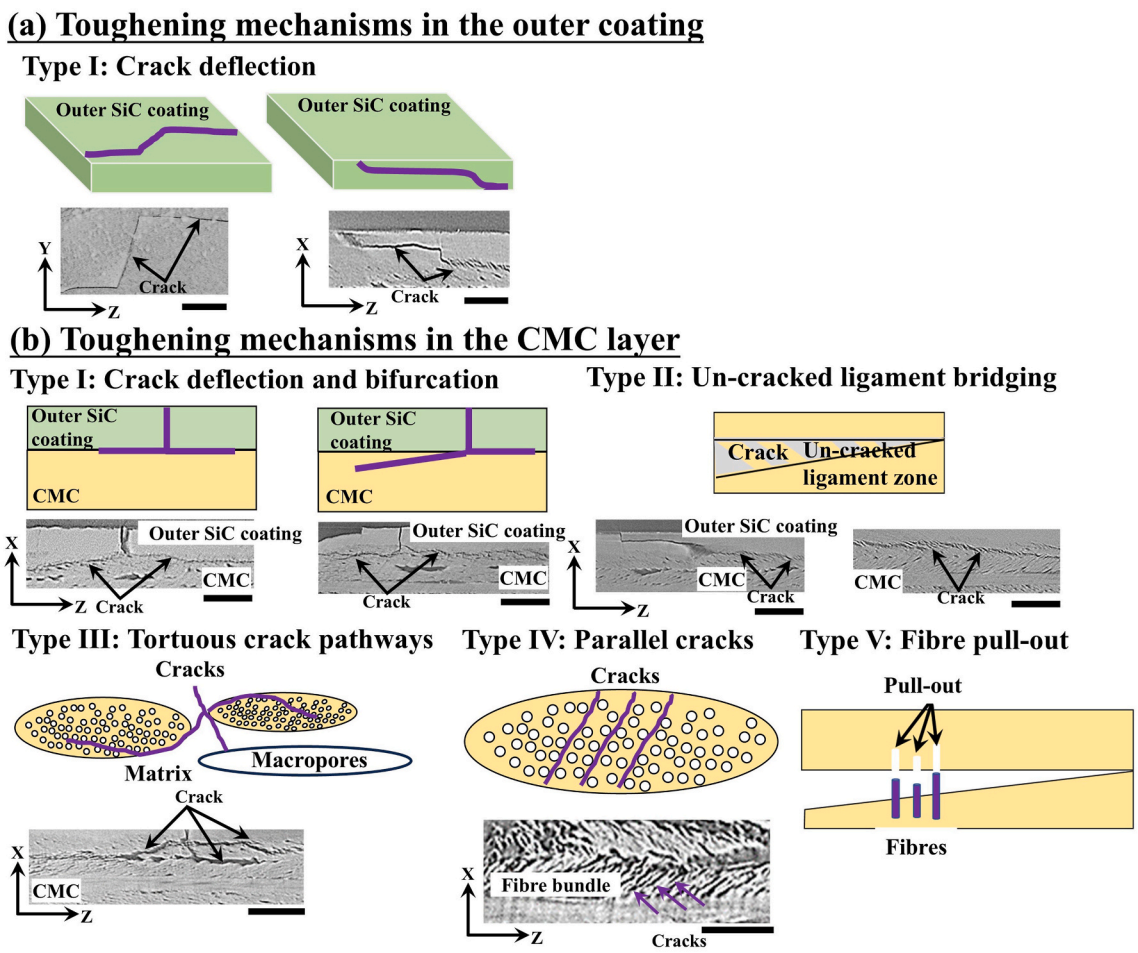


Fig. 11. Schematics and corresponding representative XCT slices of the crack toughening mechanisms. (a) mechanisms in the outer SiC coating: (Type I) deflection on the coating surface, deflection inside the coating. (b) mechanisms in the CMC layer: (Type I) crack deflection and bifurcation, (Type II) un-cracked ligament bridging, (Type III) tortuous crack pathways, (Type IV) parallel cracks in the fibre bundles and (Type V) fibre pull-out.

layers, which is consistent with differences in local structural order/crystallinity; as Drieux et al. [33] reported that the formation of smaller coherent SiC domains, increased density of grain boundaries and stacking faults resulted in similar observations to current work. These observations are used qualitatively rather than as an absolute measurement of crystallinity.

The novel bilayer coating structure may enhance the damage tolerance of the material by promoting crack deflection. Closed pores were observed near the interface between the two sub-layers (Fig. 2b), where they may act as local weak paths that facilitate crack deflection. The formation of these interfacial pores may be associated with incomplete coalescence and densification of the growing SiC crystallites during CVD deposition, potentially caused by changes in the deposition conditions between the two sub-layers. Zheng et al. [50] reported that insufficient deposition temperature or time could restrict the growth, fusion and agglomeration of SiC crystallites, resulting in incomplete coatings, whereas excessive temperature or prolonged deposition could produce coarser and less compact coatings containing voids or holes. Because gas tightness, leak rate and permeability were not measured, neither the closed-pore morphology nor the absence of an XCT-resolvable through-thickness crack should be interpreted as evidence of retained hermeticity. The lower-crystallinity sub-layer may also affect the hoop strength of the outer SiC coating, as discussed in Section 4.3. For comparison, our previous 11-sub-layer SiC coating [3] also exhibited crack deflection/bifurcation at internal coating interfaces. However, unlike the present bilayer outer coating, which shows a through-thickness elastic-modulus gradient, the multi-layer coating exhibited nearly uniform hardness and elastic modulus despite a residual-stress gradient across the coating's thickness [3]. Direct performance ranking is not appropriate because the two studies differ in defect state, coating thickness, CMC architecture and other material characteristics.

In terms of the underlying CMC substrate, the present gradient 2D-braided substrate exhibited interconnected macropore regions, in contrast to the more isolated macropores reported for similar 3D-orthogonally braided materials [2], one representative example is presented in Fig. S10 in the Supplementary Materials.

In current work, during C-ring loading at both RT and 1200°C in Ar, the propagating XCT-resolvable cracks were observed to connect with these interconnected pore regions and to redirect or terminate near fibre-bundle interfaces, with the maximum observed penetration located near the interface between fibre-bundle layers II and III. These spatial correlations suggest that the architecture-associated pore morphology may contribute to local crack-path redistribution under the present C-ring loading conditions. In comparison, for similar 3D-braided SiC_f/SiC_m materials under C-ring compression at elevated temperatures (up to 1200°C) in Ar atmosphere, through-thickness cracks were commonly reported [2], [3]. Accordingly, the observed crack arrest and absence of an XCT-resolvable through-thickness crack may reflect the combined effects of several non-independent factors, including fibre-bundle orientation, morphology and connectivity of porosity, interfaces, coating/CMC interfacial properties, the bilayer-coating sub-layer interface, constituent-property heterogeneity, local residual stresses, and the bending-dominated stress gradient and free-edge effects inherent to the C-ring configuration. It should also be noted that

crack deflection or interfacial delamination does not necessarily imply improved overall structural integrity. Although such processes can redirect a crack away from direct through-thickness penetration, they may simultaneously increase local coating/CMC interfacial damage or coating delamination. However, because no matched architecture or pore-controlled specimen was tested, these observations do not establish the gradient architecture or macropore connectivity as the sole cause of crack arrest or as evidence of superior damage tolerance relative to 3D-braided systems.

We emphasize that the formation of interconnected macropores does not mean the total porosity of the cladding material is high. From open literature, the total porosities of similar SiC_f-SiC_m cladding system is reported to be 8.7% to 20% [2], [8], [29], [31], [32], [51], [52], [53], with detailed information for these materials summarized in Table S5. In this work, the porosity is ~9.6% based on the XCT images, which is well within the normal range of reported porosity. In the CMC substrate, PyC coatings were deposited around the fibre bundles, as well as at the interface between outer SiC coating/CMC layer, Fig. 3. This is not commonly reported in similar SiC_f-SiC_m cladding materials [1], [4], [13], [15], [16]. In this study, crack deflection, bifurcation and fibre pull-out occurred in spatial proximity to these heterogeneous interfacial regions. This observation is consistent with the established role of compliant PyC interphases in facilitating interfacial debonding and sliding. However, without a matched PyC-free control, its individual contribution cannot be isolated from the other microstructural and loading factors.

4.2. Interpretation of the local properties

Nanoindentation revealed distinct local mechanical responses among the coating, matrix and fibre (Table 1). The outer coating exhibits higher hardness and elastic modulus than the CVI matrix and HI-NICALON™-Type-S fibre. This difference is expected considering the different processing routes and resulting microstructures of these constituents. The outer coating is deposited as a dense monolithic SiC layer [8], whereas the surrounding matrix is formed through the CVI process, which may introduce residual porosity associated with the infiltration process [2], [54]. In addition, SiC fibres possess distinct fibre-scale microstructures and are designed to provide reinforcement rather than bulk ceramic stiffness. Therefore, the higher local mechanical properties of the outer coating are likely associated with its dense monolithic structure, reduced heterogeneity and crystallographic characteristics [8], [55].

Within the bilayer coating, the elastic modulus decreased from the inner to the outer sub-layer, whereas hardness remained comparatively uniform through the thickness (Fig. 4). This property gradient coincides with the different columnar-grain morphologies observed by SEM and the differences in SiC TO-band shape/broadening observed by Raman spectroscopy (Fig. 2). Previous studies have shown that the elastic properties of CVD-SiC coatings can vary with crystallinity and microstructural characteristics, while the hardness remained similar [56]. These suggest that deposition-related microstructural differences may contribute to the measured property gradient. However, the present measurements do not resolve the specific nanoscale compositional or crystallographic origin of this difference. Dedicated transmission electron microscopy (TEM) or energy-dispersive X-ray spectroscopy (EDS) or equivalent nanoscale characterization would be required to distinguish the respective effects of deposition history, chemistry and grain-scale structure.

The HI-NICALON™-Type-S fibre exhibited significantly lower hardness and elastic modulus than the other SiC-based components, consistent with previous observations from similar SiC_f/SiC_m materials [2], [54]. Such low hardness and elastic modulus values could be attributed to the presence of carbon phase (commonly be detected by Raman spectroscopy [54], which has significantly lower hardness and modulus compared with SiC phase) inside this type of fibre [2]. In this study, carbon Raman peaks: disorder mode (D) peak (~1360 cm^{-1}), graphitic mode (G) peak (~1584.5 cm^{-1}) and D' peak (~1620 cm^{-1}) were detected in the SiC fibres (Fig. 12), confirming the presence of carbon-phase in the present fibres.

After the 1200°C C-ring compression tests (with a total test duration of ~100 min), increased hardness and elastic modulus values were measured for the outer coating, SiC matrix and fibres compared with the as-received materials (Table 1). These changes indicate that the local mechanical response of the constituent phases was modified during the high-temperature mechanical testing process. However, it should be noted that the post-tested specimens experienced both thermal exposure and mechanical loading, and therefore the measured changes cannot be attributed to temperature alone.

For the HI-NICALON™-Type-S fibres, previous studies have demonstrated that high-temperature exposure can induce pronounced microstructural evolution, including β-SiC crystallization and changes in carbon-related phases. Tarfaoui et al. [57] reported that such structural evolution may modify the local mechanical response of the fibres after thermal treatment. Similarly, Bhatt et al. [10] reported that high-temperature exposure of SiC_f/SiC_m composites could reduce structural disorder and promote microstructural stabilization through improved SiC stoichiometry and annealing of structural defects. These observations provide possible explanations for the changes measured in the present study.

For the CVD-SiC coating and SiC matrix, the measured increases in hardness and elastic modulus may also be associated with changes in microstructure, defect populations and residual stress states during high-temperature exposure. Previous nanoindentation investigations on heat-treated SiC-based materials (including 2D woven CVI SiC_f/SiC_m materials [10] and CVD SiC layers in tristructural-isotropic (TRISO) fuel particles [58]) have reported variations in hardness and elastic modulus after thermal treatment, suggesting that changes in crystallinity and stress state can influence local mechanical measurements. Additionally, residual stress relaxation may also contribute because manufacturing-induced residual stresses are commonly present in the individual components in SiC_f/SiC_m materials [2].

Nevertheless, the present results do not establish a specific causal mechanism for the measured property changes. Since the post-tested specimens experienced simultaneous thermal exposure and mechanical loading, while no unloaded thermally exposed control was included, the individual contributions of temperature, mechanical stress, damage evolution, defect annealing and residual stress relaxation cannot be separated. Therefore, the measured increase in hardness and elastic modulus should be interpreted as a combined response of the constituent phases after high-temperature mechanical testing rather than direct evidence of temperature-induced strengthening.

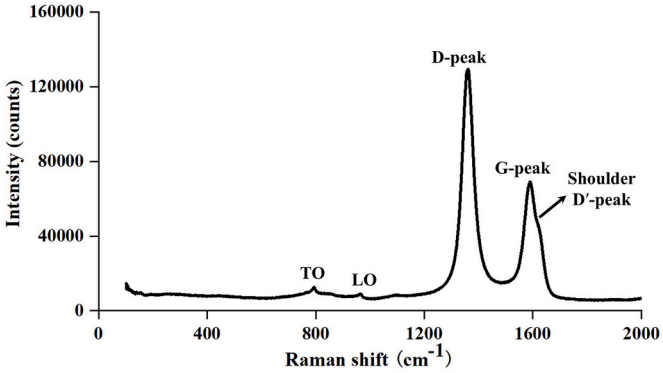


Fig. 12. Typical Raman spectra collected in the centre of fibre.

4.3. Nominal C-ring stresses associated with coating cracking and peak load

In this study, the practical interpretation of the present C-ring results also requires consideration of the specimen geometry. An intact fuel-cladding tube subjected to internal gas pressure develops predominantly tensile circumferential membrane stress, whereas diametral compression of an open C-ring produces a bending-dominated stress state with the maximum tensile hoop stress located near the outer surface and a substantial stress gradient through the wall-thickness [59], [60]. The free edges introduced by sectioning the tube also reduce the circumferential constraint relative to an intact tubular geometry. Consequently, the C-ring configuration provides a convenient comparative method for studying hoop-oriented damage evolution, particularly for high-temperature *in situ* XCT, but it does not reproduce the complete stress state of an internally pressurised cladding tube. The specimen geometry may therefore influence the location of crack initiation, subsequent stress redistribution and the relative tendency for coating cracking, interfacial deflection and through-wall propagation. The present results should thus be interpreted as the damage and failure behaviour under the tested C-ring loading configuration; direct assessment of intact-cladding performance would require complementary internal-pressure or other tube-level testing. It is again worth noting that comparison of the measured strength between RT and 1200°C is based on two specimens for each condition. Therefore, the observed difference should be considered as a measured trend within the investigated specimens rather than a statistically validated temperature-dependent change.

In open literature, published data for the nominal stress associated with first outer-coating cracking are limited, as most C-ring studies report only peak-load-derived nominal hoop stress. One exception is Yuan et al. [2], who reported such stress of a 3D SiC_f-SiC_m cladding (with ~200 μm thickness of outer monolithic coating) under C-ring compression tests in Ar: ~129 MPa at RT and ~201 MPa at 1200°C. Additional values extracted from published load/stress–displacement curves for similar coated SiC_f-SiC_m claddings are summarized in Table S6 and fall within ~169–240 MPa. In the present material, the corresponding nominal stresses of coating crack initiation were 54.9 ± 3.0 MPa at RT and 40.9 ± 1.9 MPa at 1200°C in Ar. The lower values may partly reflect differences in outer coating thickness and microstructure (~120 μm *vs.* 200-300 μm in other reported SiC_f-SiC_m claddings tested by C-ring compression) [2], [3], [37]. Drieux et al. [33], for instance, reported substantially different C-ring strengths for bilayer CVD-SiC tubes with different proportions of higher- and lower-crystallinity SiC. Because these systems also differ in geometry and material configuration, the comparison is contextual rather than a direct strength ranking.

The present C-ring results show comparable maximum nominal hoop stress levels at RT and 1200°C in Ar within the limited specimen set. This observation is consistent with independent high-temperature C-ring measurements by Shapovalov et al. [37], who reported retention of RT strength in nuclear-grade tubular SiC_f-SiC_m tested in flowing Ar to temperatures approaching 1900°C. However, their apparent strength increase at the highest temperatures was within relatively large experimental scatter, and other studies have reported both strength retention and strength degradation depending on fibre type, processing route, interphase condition and testing environment [2], [37], [61]. Therefore, the present results should not be interpreted as evidence that SiC_f-SiC_m cladding generally exhibits unchanged or increased strength at 1200°C. Rather, they indicate that the present material retained comparable maximum nominal C-ring stress under the specific short-duration, non-oxidizing Ar conditions investigated here.

Lastly, the maximum nominal hoop stress in this work is much lower than several 3D-braided SiC_f/SiC_m materials under same C-ring compression tests from open literature: 169 MPa to 418 MPa at RT [2], [60], [62], and 231 MPa to 239 MPa at 1200°C [2], [3]. This difference should not be attributed uniquely to fibre architecture because the reported systems also differ in fibre orientation and volume fraction, porosity, coating configuration, interfacial structure, processing history and specimen geometry. The comparison is therefore contextual rather than a matched architectural comparison. Nevertheless, three non-exclusive factors may contribute to the lower maximum nominal hoop stress measured here.

(i) Compared with 3D architectures containing substantial through-thickness reinforcement, the present gradient 2D-braided architecture contains little through-thickness fibre reinforcement. Consequently, local interlaminar and radial stresses generated during crack propagation may be carried to a greater extent by the SiC matrix and interfaces, whereas through-thickness fibre bundles in 3D architectures can provide additional crack bridging and constrain interlaminar separation [63]. This architectural difference may therefore contribute to a lower resistance to through-thickness damage and, potentially, to the lower peak load measured in the present specimens. (ii) PyC-containing interfacial regions were observed around fibre bundles, and crack deflection and bifurcation frequently occurred nearby. Interfacial debonding and sliding associated with these regions may redistribute local load and reduce simultaneous recruitment of all fibre bundles before peak load, thereby contributing to a lower measured peak load. (iii) Previous studies of 3D SiC_f/SiC_m cladding under C-ring compression have reported cracks propagating through the total wall-thickness after peak load [2], [60], [62]. In the present specimens, XCT-resolvable cracks instead interacted with interconnected inter-bundle macropores, and the deepest crack fronts remained near the layer-II/layer-III interface without forming an XCT-resolvable through-thickness crack within the investigated volume (Figs. 7 and 9). This spatial relationship suggests that the macropore network may contribute to crack-path redistribution and non-uniform load sharing among fibre-bundle layers. These interpretations remain mechanistic hypotheses because no matched architectural, PyC-free or pore-controlled specimens were tested; the individual contributions cannot be separated from constituent heterogeneity or the C-ring stress field.

4.4. Summary of failure processes at RT and 1200°C

For clarity, the progressive failure processes identified from the *in situ* XCT observations are summarized schematically in Fig. 13, where the four characteristic loading stages are linked to coating cracking, crack penetration into the CMC, crack–microstructure interaction and the final investigated post-peak state. No obvious motion-related blurring was observed, although minor or sub-resolution damage evolution during individual acquisitions cannot be excluded. At RT, the observed failure process can be summarized in four stages: (i) elastic loading before the first XCT-resolvable crack; (ii) initiation of a principal crack in the outer SiC coating, accompanied by deflection within the bilayer coating and initial penetration into the CMC and fibre pull-out; (iii) further penetration and branching within the CMC, together with continued damage accumulation; and (iv) increased crack opening and penetration, with the deepest XCT-resolvable crack front remaining near the interface between fibre-bundle layers II and III. No XCT-resolvable through-thickness crack was observed within the investigated volume. The same overall four-stage sequence was observed at 1200°C in Ar, but two differences were evident. First, the nominal hoop stress associated with outer-coating crack initiation was lower than at RT, and the principal coating crack extended across the observable specimen width once it became XCT-resolvable. Second, post-mortem fibre pull-out was less extensive than at RT (Fig. 10). Thus, elevated temperature modified the manifestation of the same overall hierarchical failure sequence rather than producing a fundamentally different failure mechanism.

Compared with our previous 3D-braided SiC_f/SiC_m claddings tested

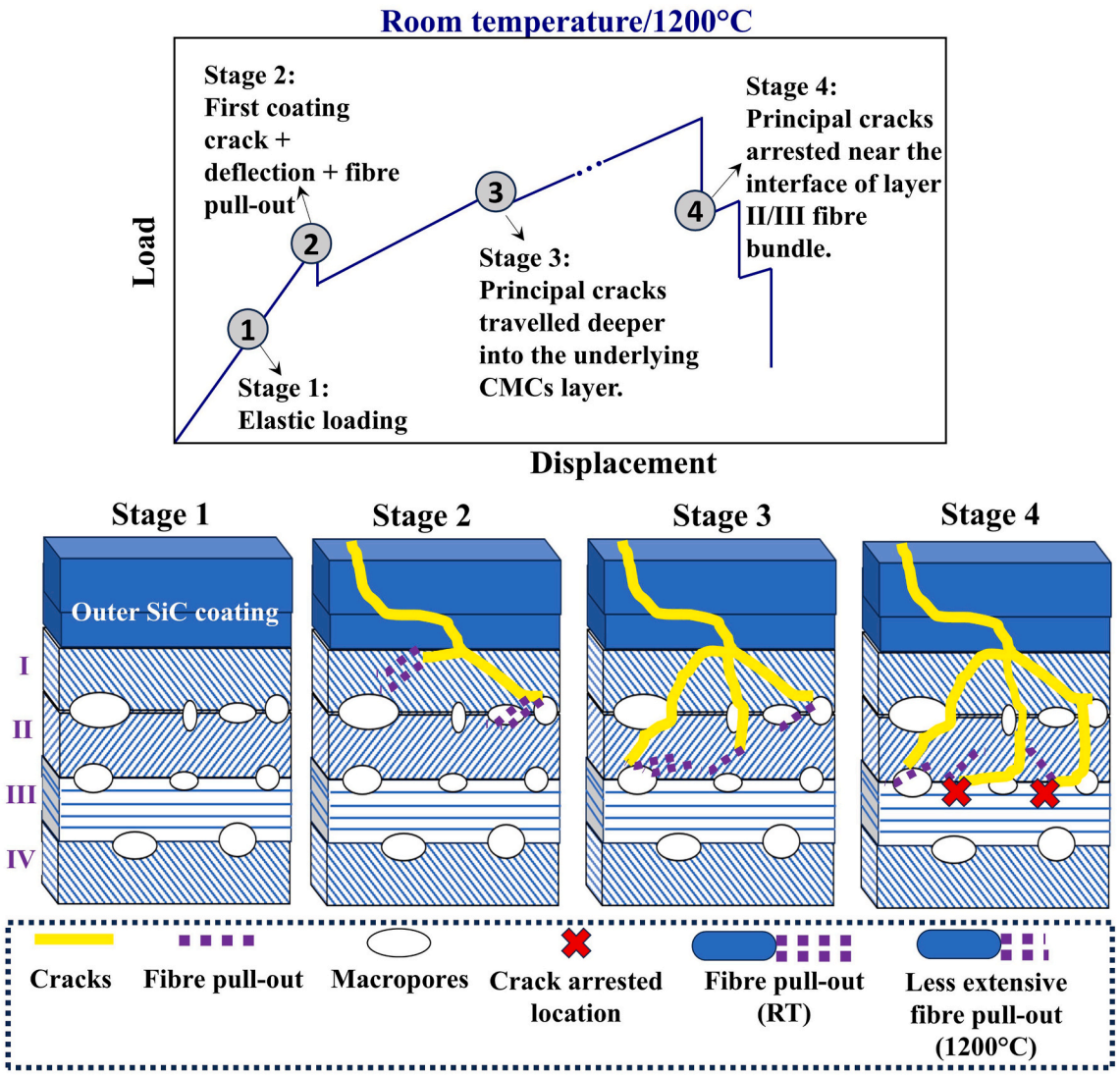


Fig. 13. Schematic summary of the progressive failure process of the SiC_f/SiC_m cladding under C-ring compression at RT and 1200°C in Ar. The four characteristic stages distinguish initial outer-coating crack initiation, subsequent coating cracking and interfacial delamination, matrix/fibre-bundle damage within the CMC substrate, and the final investigated post-peak state with arrest of the principal XCT-resolvable crack near the interface between fibre-bundle layers II and III. The schematic also illustrates the comparatively more extensive fibre pull-out observed post mortem at RT and less extensive fibre pull-out after testing at 1200°C. The schematics are not drawn to scale.

under similar C-ring conditions [2], [3], the present material exhibited a different sequence of coating/CMC crack interaction. These differences are treated as material-specific damage-path characteristics rather than evidence of a general architectural advantage, because the compared systems differ in coating design, fibre architecture, porosity and other material characteristics.

Furthermore, less extensive visible fibre pull-out was observed after testing at 1200°C than at RT. One possible explanation is an increase in the effective resistance to fibre/interphase sliding at elevated temperature [64], [65]. According to shear-lag descriptions of fibre-reinforced brittle-matrix composites, increased interfacial frictional resistance reduces the characteristic load-transfer length and may promote fibre fracture closer to the matrix-crack plane [64], [65]. Recently, Jin et al. (2020) [66] similarly reported a transition from fibre pull-out to fibre breakage of SiC_f/SiC_m composites at temperatures around and above 1200°C, which they attributed to increased radial clamping at the fibre–matrix interface associated with changes in residual radial stress. A similar change in interfacial constraint among the Hi-Nicalon™ Type-S fibres, PyC interphase and CVI-SiC matrix may therefore have contributed to the reduced pull-out observed here. This interpretation is also consistent with Buet et al. [67], who demonstrated that the PyC interphase characteristics directly affect interfacial shear stress and fibre pull-out length in Hi-Nicalon-S/SiC composites. As the experiments in this work were performed in Ar gas, oxidation-induced bonding of the PyC interphase is unlikely to be the main reason. Nevertheless, because the interfacial shear strength was not measured directly at 1200°C, the less extensive/reduced visible fibre pull-out should be interpreted as evidence of altered interfacial load transfer rather than conclusive proof of increased interfacial strength.

The principal RT/1200°C comparison in this study was intentionally performed in high-purity Ar to provide a non-oxidizing baseline and to reduce the influence of environmental oxidation on the observed thermo-mechanical response. This condition therefore does not reproduce the complete environment expected during an accident scenario. To examine the sensitivity of the failure behaviour to an oxidizing environment, two additional specimens were tested at 1200°C in air, with the detailed results provided in the Supplementary Materials (Fig. S11–S14 and Table S7). The maximum nominal hoop stresses of the air-tested specimens were 49.57 and 54.21 MPa, compared with 75.31 and 85.66 MPa for the specimens tested at 1200°C in Ar. Given the

limited number of specimens, this comparison is descriptive rather than a statistically established environmental effect. A similar environmental sensitivity was reported by Shapovalov et al. [37] in their SiC_f/SiC_m claddings under C-ring compression in air up to 1100°C. The peak load decreased with increasing temperature: ~15 N at RT, ~12 N at 600°C and ~6 N at 1100°C. They suggested that such degradation of strength was caused by the oxidation of PyC interphases surrounding fibres [68], which reduced the potential for crack deflection and fibre sliding at the interphase area. Thereby concentrating stress within the fibres at such area, promoted fibre fracture and ultimately reduced the overall composite strength. In the present study, the characteristic carbon Raman bands from PyC-containing interfacial regions were no longer detected after testing at 1200°C in air (Fig. S14), consistent with substantial oxidation or loss of the PyC interphase, whereas these carbon-related features remained detectable after testing at 1200°C in Ar. This difference is consistent with environmental degradation of the PyC-containing interfaces in air.

More importantly, the crack-evolution pathways also differed between the two environments. At RT and 1200°C in Ar, crack deflection was clearly resolved on the outer-coating surface and within the bilayer outer coating (Figs. 7 and 9), whereas comparable crack deflection was not clearly observed at 1200°C in air within the present XCT resolution (Fig. S12 and Fig. S13). The air-tested specimens instead exhibited a comparatively more direct crack path, with XCT-resolvable cracking ultimately extending through the complete wall-thickness of the cladding (Fig. S13). These observations demonstrate that the testing environment can modify the interfacial condition and subsequent damage-evolution pathway. However, the present data do not isolate a single mechanism responsible for the reduced apparent crack deflection within the outer SiC coating, and this difference should therefore not be attributed exclusively to PyC oxidation. Finally, high-temperature air does not reproduce the steam-rich oxidizing environment relevant to LOCA conditions. Dedicated high-temperature steam/oxidation testing, together with leak-rate or permeability measurements and intact-tube internal-pressure testing, will therefore be required to determine whether the damage evolution observed here translates to functional cladding performance under accident-relevant conditions.

5. Conclusions

The failure processes of a SiC-coated gradient 2D-braided nuclear-grade SiC_f/SiC_m cladding material were investigated under C-ring compression at RT and 1200°C in Ar using *in situ* synchrotron XCT, supported by SEM, Raman spectroscopy and nanoindentation. The main conclusions are as follows:

(i) The bilayer CVD-SiC outer coating exhibited a through-thickness elastic-modulus gradient and distinct sub-layer morphologies. Crack deflection was repeatedly observed near the interface between the two coating sub-layers at both RT and 1200°C, identifying this interface as an important feature in the hierarchical crack-transfer process.

(ii) After penetrating the coating/CMC interface, XCT-resolvable cracks underwent redirection and branching in spatial association with fibre-bundle interfaces and interconnected inter-bundle pores. The deepest crack fronts remained near the interface between fibre-bundle layers II and III, and no XCT-resolvable through-thickness crack was observed within the investigated Ar-tested volumes. These observations establish spatial associations rather than a causal advantage of the gradient 2D-braided architecture, because no matched architectural control was tested.

(iii) The nominal hoop stresses associated with outer-coating crack initiation were lower at 1200°C than at RT, whereas the maximum nominal hoop stresses were comparable within the limited specimen set: 77.3 ± 2.7 MPa at RT and 80.5 ± 7.3 MPa at 1200°C in Ar (n = 2) per condition. The same overall four-stage failure sequence was observed at both temperatures, although the 1200°C specimens showed less extensive visible fibre pull-out. Modestly higher post-test local hardness and elastic modulus values were also measured after the 1200°C test, but these differences cannot be attributed solely to temperature because no thermally exposed, mechanically unloaded control was available. Possible contributors include defect annealing, microstructural/crystallinity changes and redistribution or relaxation of residual stresses during the combined high-temperature mechanical test; however, their individual contributions cannot be separated by the present experimental design.

(iv) The supplementary 1200°C-air tests showed a lower mean maximum nominal hoop stress (~51.9 MPa) than the corresponding 1200°C-Ar tests (~80.5 MPa), together with a more direct crack path and XCT-resolvable through-wall cracking. These observations demonstrate strong environmental sensitivity of the failure process and show that the Ar results should not be generalized to oxidizing accident environments.

Overall, the *in situ* XCT observations reveal a hierarchical crack-transfer sequence from the bilayer coating, across coating interfaces and into the gradient braided CMC substrate, with temperature and environment modifying its manifestation. Hermeticity, leak rate and permeability were not evaluated; therefore, the absence of an XCT-resolvable through-thickness crack under the Ar conditions should not be interpreted as retained gas tightness or functional cladding integrity. Future validation requires intact-tube internal-pressure, leak/permeability, high-temperature steam/oxidation and irradiation/post-irradiation testing.

CRediT authorship contribution statement

Guanjie Yuan: Writing – original draft, Investigation, Formal analysis. **Qiance Zhang:** Writing – review & editing. **Edward Lahoda:** Writing – review & editing, Resources. **Toshiki Nishimura:** Writing – review & editing, Resources. **Masaru Ukai:** Writing – review & editing, Resources. **Toshiaki Takada:** Writing – review & editing, Resources. **Peng Xu:** Writing – review & editing, Resources. **Robert O. Ritchie:** Writing – review & editing. **Dong Liu:** Writing – review & editing, Resources, Methodology, Funding acquisition, Conceptualization, Data curation, Project administration, Supervision, Formal analysis.

Declaration of competing interest

The authors declare that they have no known competing financial interests or personal relationships that could have appeared to influence the work reported in this paper.

Acknowledgements

This research was funded in whole, or in part, by the UKRI [ST/W001683/1, EP/T000368/1, UKRI1795]. For the purpose of Open Access, the author has applied a CC BY public copyright licence to any Author Accepted Manuscript version arising from this submission. The authors also acknowledge the use of the X-ray synchrotron microtomography beamline (8.3.2) at the Lawrence Berkeley National Laboratory's Advanced Light Source, which is supported by the Office of Science of the U.S. Department of Energy under contract no. DE-AC0205CH11231. Thanks are also due to Dr. Dula Parkinson for help with these synchrotron tomography experiments.

Appendix A. Supplementary data

Supplementary data to this article can be found online at https://doi.org/10.1016/j.compositesb.2026.114300.

Data availability

The raw data and processed data required to reproduce these results in current work are available on reasonable request from the corresponding author.

References

[1] Ramachandran K, Bear JC, Jayaseelan DD. Oxide-based ceramic matrix composites for high-temperature environments: a review. Adv Eng Mater 2025;27(7):2402000.
[2] Yuan G, Forna-Kreutzer JP, Xu P, et al. In situ high-temperature 3D imaging of the damage evolution in a SiC nuclear fuel cladding material. Mater Des 2023;227:111784.
[3] Yuan G, Cook DH, Barnard H, et al. Improved damage tolerance of SiC-based nuclear fuel cladding with novel multi-layered SiC coating design at 1200° C. Mater Des 2025;256:114260.
[4] Daspit JT, Neiderer JM, Mohammadi-Koumleh F, et al. Mechanics of an inner monolithic SiC layer in multilayer SiC/SiC composite tubes. Compos B Eng 2026:113446.
[5] Zhang R, Liu T, He Y, et al. Experimental study on failure behavior of triplex SiC composite tubes under high strain rate internal pressurization. J Eur Ceram Soc 2026:118360.
[6] Deck CP, Khalifa HE, Sammuli B, et al. Fabrication of SiC–SiC composites for fuel cladding in advanced reactor designs. Prog Nucl Energy 2012;57:38–45.
[7] Katoh Y, Ozawa K, Shih C, et al. Continuous SiC fiber, CVI SiC matrix composites for nuclear applications: properties and irradiation effects. J Nucl Mater 2014;448(1–3):448–76.
[8] Deck CP, Jacobsen GM, Sheeder J, et al. Characterization of SiC–SiC composites for accident tolerant fuel cladding. J Nucl Mater 2015;466:667–81.
[9] Li X, Yan W, Dai Y, et al. Study on the circumferential tensile behavior of SiCf/SiC composite cladding tubes across a broad temperature range: high temperature interface enhancement effect from a cross-scale perspective. Ceram Int 2025;51(2):2566–76.
[10] Bhatt RT, Eldridge JI. Heat treatment effects on microstructure and properties of CVI SiC/SiC composites with Sylramic™-iBN SiC fibers. J Eur Ceram Soc 2023;43(6):2376–87.
[11] Ubaid J, Alaleeli M, Alameri SA, et al. Thermomechanical analysis of SiC-based duplex claddings with varying thickness ratio for accident-tolerant nuclear fuel systems. Energy Convers Manag X 2024;23:100672.
[12] Wang H, Liu S, Li Y, et al. Modeling of the thermomechanical behavior of braided SiCf/SiC composite cladding tube during irradiation. J Nucl Mater 2025;608:155723.
[13] Koyanagi T, Katoh Y, Nozawa T, et al. Recent progress in the development of SiC composites for nuclear fusion applications. J Nucl Mater 2018;511:544–55.
[14] Nance J, Subhash G, Sankar B, et al. Measurement of residual stress in silicon carbide fibers of tubular composites using Raman spectroscopy. Acta Mater 2021;217:117164.
[15] Katoh Y, Ozawa K, Hinoki T, et al. Mechanical properties of advanced SiC fiber composites irradiated at very high temperatures. J Nucl Mater 2011;417(1–3):416–20.
[16] Karakoc O, Koyanagi T, Nozawa T, et al. Fiber/matrix debonding evaluation of SiCf/SiC composites using micropillar compression technique. Compos B Eng 2021;224:109189.
[17] Igawa N, Taguchi T, Nozawa T, et al. Fabrication of SiC fiber reinforced SiC composite by chemical vapor infiltration for excellent mechanical properties. J Phys Chem Solid 2005;66(2–4):551–4.
[18] Chen Y, Gélébart L, Chateau C, et al. Crack initiation and propagation in braided SiC/SiC composite tubes: effect of braiding angle. J Eur Ceram Soc 2020;40(13):4403–18.
[19] Liu G, Zhu W, Wang C, et al. Advances in 3D printing of SiC ceramic matrix composites: a comprehensive review. Compos B Eng 2025:113342.
[20] Xie F, Chen Z, Qiao Z, et al. An asymmetric 2D braiding strategy for balancing hoop and axial strength in SiC/SiC composite nuclear fuel cladding. Compos B Eng 2025:113013.
[21] Sauder C. Ceramic matrix composites: nuclear applications. Ceramic matrix composites: materials, modeling and technology 2014:609–46.
[22] Wei C, Liang S, Zhang C, et al. Multi-scale design and mechanical enhancement of SiCf/SiC composite cladding for accident-tolerant fuel. J Mater Res Technol 2025;36:4427–44.
[23] Morscher GN, Yun HM, DiCarlo JA. In-plane cracking behavior and ultimate strength for 2D woven and braided melt-infiltrated SiC/SiC composites tensile loaded in off-axis fiber directions. J Am Ceram Soc 2007;90(10):3185–93.
[24] Morscher GN, DiCarlo JA, Kiser JD, et al. Effects of fiber architecture on matrix cracking for melt-infiltrated SiC/SiC composites. Int J Appl Ceram Technol 2010;7(3):276–90.
[25] Jacobsen TK, Brøndsted P. Mechanical properties of two plain-woven chemical vapor infiltrated silicon carbide-matrix composites. J Am Ceram Soc 2001;84(5):1043–51.
[26] Yang Z, Pang K, Lei X, et al. A quantitative representation of damage and failure response of three-dimensional textile SiC/SiC ceramics matrix composites subjected to flexural loading. J Eng Mater Technol 2023;145(3):031001.
[27] Liu C, Chen Y, Shi D, et al. In situ investigation of failure in 3D braided SiCf/SiC composites under flexural loading. Compos Struct 2021;270:114067.
[28] Zhao S, Zhou X, Yu J, et al. Fabrication and characterization of 2.5 D and 3D SiCf/SiC composites. Fusion Eng Des 2013;88(9–10):2453–6.
[29] Rohmer E, Martin E, Lorrette C. Mechanical properties of SiC/SiC braided tubes for fuel cladding. J Nucl Mater 2014;453(1–3):16–21.
[30] Zhang J, Khalifa HE, Deck C, et al. Thermal diffusivity measurement of curved samples using the flash method[C]//Ceramic materials for energy applications V: a collection of papers presented at the 39th International Conference on Advanced Ceramics and Composites. Hoboken, NJ, USA: John Wiley & Sons, Inc.; 2015. p. 43–56.
[31] Bernachy-Barbe F, Gélébart L, Bornert M, et al. Anisotropic damage behavior of SiC/SiC composite tubes: multiaxial testing and damage characterization. Compos Appl Sci Manuf 2015;76:281–8.
[32] Kim D, Lee HG, Park JY, et al. Fabrication and measurement of hoop strength of SiC triplex tube for nuclear fuel cladding applications. J Nucl Mater 2015;458:29–36.
[33] Drieux P, Chollon G, Jacques S, et al. Synthesis and characterization of monolithic CVD-SiC tubes. J Eur Ceram Soc 2016;36(8):1873–83.
[34] Saucedo-Mora L, Lowe T, Zhao S, et al. In situ observation of mechanical damage within a SiC-SiC ceramic matrix composite. J Nucl Mater 2016;481:13–23.
[35] Yuan G, Ševeček M, Cook D, et al. Investigation of the temperature-dependent failure processes in PVD Cr-coated ZIRLO nuclear fuel cladding using in situ X-ray micro-tomography imaging. Surf Coating Technol 2025;512:132376.
[36] Kim J, Joung SH, Lee Y. Effect of Cr coating on the mechanical integrity of Accident Tolerant Fuel cladding under ring compression test. J Nucl Mater 2023;585:154603.
[37] Shapovalov K, Jacobsen GM, Shih C, et al. C-ring testing of nuclear grade silicon carbide composites at temperatures up to 1900 C. J Nucl Mater 2019;522:184–91.
[38] Yook H, Shirvan K, Phillips B, et al. Post-LOCA ductility of Cr-coated cladding and its embrittlement limit. J Nucl Mater 2022;558:153354.
[39] Ott LJ, Robb KR, Wang D. Preliminary assessment of accident-tolerant fuels on LWR performance during normal operation and under DB and BDB accident conditions. J Nucl Mater 2014;448(1–3):520–33.
[40] Yuan G, Forna-Kreutzer JP, Ell J, et al. In situ X-ray computed micro-tomography imaging of failure processes in Cr-coated Zircaloy nuclear fuel cladding materials. Mater Des 2023;234:112373.
[41] Oliver WC, Pharr GM. An improved technique for determining hardness and elastic modulus using load and displacement sensing indentation experiments. J Mater Res 1992;7(6):1564–83.
[42] ASTM Standard C1323-26. Standard test method for ultimate strength of advanced ceramics with diametrally compressed C-Ring specimens at ambient temperature. West Conshohocken, PA: ASTM International; 2016. https://doi.org/10.1520/C1323-16.2.
[43] Liu D, Gludovatz B, Barnard HS, et al. Damage tolerance of nuclear graphite at elevated temperatures. Nat Commun 2017;8(1):15942.
[44] Haboub A, Bale HA, Nasiatka JR, et al. Tensile testing of materials at high temperatures above 1700 C with in situ synchrotron X-ray micro-tomography. Rev Sci Instrum 2014;85(8).
[45] Yakovlev MA, Vanselow DJ, Ngu MS, et al. A wide-field micro-computed tomography detector: micron resolution at half-centimetre scale. Synchrotron Radiation 2022;29(2):505–14.
[46] Gürsoy D, De Carlo F, Xiao X, et al. TomoPy: a framework for the analysis of synchrotron tomographic data. Synchrotron Radiation 2014;21(5):1188–93.
[47] Yuan G, Zhang Q, Barnard H, et al. Effects of outer coating thickness on the failure strength of a SiC-based nuclear-fuel cladding up to 1200° C. Mater Des 2026:116869.
[48] Forna-Kreutzer JP, Ell J, Barnard H, et al. Full-field characterisation of oxide-oxide ceramic-matrix composites using X-ray computed micro-tomography and digital volume correlation under load at high temperatures. Mater Des 2021;208:109899.
[49] Jiang M, Ell J, Barnard H, et al. On the reduced damage tolerance of fine-grained nuclear graphite at elevated temperatures using in situ 4D tomographic imaging. Carbon 2024;222:118924.
[50] Zheng X, Liu Y, Fu S, et al. Effect of deposition temperature and time on microstructure of CVD SiC coating on diamond particles. Surf Interfaces 2021;24:101076.
[51] Alva L, Shapovalov K, Jacobsen GM, et al. Experimental study of thermo-mechanical behavior of SiC composite tubing under high temperature gradient using solid surrogate. J Nucl Mater 2015;466:698–711.
[52] Shapovalov K, Jacobsen GM, Alva L, et al. Strength of SiCf-SiCm composite tube under uniaxial and multiaxial loading. J Nucl Mater 2018;500:280–94.
[53] Singh G, Gonczy S, Deck C, et al. Interlaboratory round robin study on axial tensile properties of SiC-SiC CMC tubular test specimens. Int J Appl Ceram Technol 2018;15(6):1334–49.
[54] Frazer D, Abad MD, Krumwiede D, et al. Localized mechanical property assessment of SiC/SiC composite materials. Compos Appl Sci Manuf 2015;70:93–101.
[55] Snead LL, Nozawa T, Katoh Y, et al. Handbook of SiC properties for fuel performance modeling. J Nucl Mater 2007;371(1–3):329–77.
[56] Zhou W, Long Y. Mechanical properties of CVD-SiC coatings with Si impurity. Ceram Int 2018;44(17):21730–3.
[57] Tarfaoui M, Martynková GS, Daly M, et al. Thermal treatment effects on the microstructure and mechanical response of Hi-Nicalon SiC fibers. Ceram Int 2025.
[58] Rohbeck N, Xiao P. Evaluation of the mechanical performance of silicon carbide in TRISO fuel at high temperatures. Nucl Eng Des 2016;306:52–8.
[59] Embree TL, Segall AE. Evaluation of the uniaxiality of the stress state in C-ring fracture strength specimens. J Test Eval 2004;32(2):153–60.
[60] Jacobsen GM, Stone JD, Khalifa HE, et al. Investigation of the C-ring test for measuring hoop tensile strength of nuclear grade ceramic composites. J Nucl Mater 2014;452(1–3):125–32.

[61] Nozawa T, Kim S, Ozawa K, et al. Stress envelope of silicon carbide composites at elevated temperatures. Fusion Eng Des 2014;89(7–8):1723–7.
[62] Zhan CT, Liu YQ, Chen JP, et al. Hoop tensile properties of SiC fiber-reinforced SiC matrix composite tubes with/without CVD-SiC coating. J Eur Ceram Soc 2024;44 (14):116707.
[63] Song J, Wen W, Cui H. Experimental and numerical investigation of mechanical behaviors of 2.5 D woven composites at ambient and un-ambient temperatures. Compos Struct 2018;201:699–720.
[64] De Meyere RMG, Gale L, Harris S, et al. Optimizing the fiber push-out method to evaluate interfacial failure in SiC/BN/SiC ceramic matrix composites. J Am Ceram Soc 2021;104(6):2741–52.
[65] Evans AG, Zok FW. The physics and mechanics of fibre-reinforced brittle matrix composites. J Mater Sci 1994;29(15):3857–96.
[66] Jin E, Sun W, Liu H, et al. Effect of interface coating on high temperature mechanical properties of SiC–SiC composite using domestic Hi–Nicalon type SiC fibers. Coatings 2020;10(5):477.
[67] Buet E, Braun J, Sauder C. Influence of texture and thickness of pyrocarbon coatings as interphase on the mechanical behavior of specific 2.5 D SiC/SiC composites reinforced with Hi-Nicalon S fibers. Coatings 2022;12(5):573.
[68] Xiaowei L, Jean-Charles R, Suyuan Y. Effect of temperature on graphite oxidation behavior. Nucl Eng Des 2004;227(3):273–80.